U. S. DEPARMENT OF COMMERCE
NATIONAL OCEANIC AND ATMOSPHERIC ADMINISTRATION
NATIONAL WEATHER SERVICE
NATIONAL METEOROLOGICAL CENTER

OFFICE NOTE 410

COMPARISON OF NMC/NCAR REANALYSIS WITH 1987 FIFE DATA

ALAN K. BETTS
ATMOSPHERIC RESEARCH

SONG-YOU HONG
NRC RESEARCH ASSOCIATE

AND

HUA-LU PAN
DEVELOPMENT DIVISION

SEPTEMBER 1995

Abstract

Data from the FIFE experiment of the Summer of 1987 are used to assess the diurnal and seasonal cycles of the surface energy budget and boundary layer in the NMC/NCAR reanalysis, which uses the current (June, 1995) Medium-Range Forecast model. The seasonal agreement is quite good, reflecting the improvements in land-surface parameterizations in recent years. Detailed studies however identify several places where still further improvements in model parameterizations are possible. Clear-sky short-wave absorption and cloudiness may be underestimated in the model as has been noticed in other global models. More frequent updates of the model cloud cover (currently every 3 h) would improve the land surface interaction after the initial onset of precipitation. The model produces a realistic well-mixed boundary layer, but underestimates boundary layer deepening by entrainment. For much of the summer precipitation is close to that observed, but for a period in June and early July, the reanalysis model has excess precipitation, which comes from daytime interactions between the surface evaporation, boundary layer, and convection schemes. The model, which has a deep 2-m soil reservoir, has adequate soil moisture storage for several weeks without rain, although surface Bowen ratio fluctuates more strongly after rain than is observed. Surface evaporation is generally too high at night, especially in high winds. This analysis suggests several improvements to the model parameterizations which are currently being tested.

1. **Introduction**

The National Meteorological Center (NMC) and the National Center for Atmospheric Research (NCAR) have embarked on a Reanalysis Project that uses a frozen version of the current Medium Range Forecast (MRF) analysis/forecast system at a triangular spectral truncation of T-62 with 28 levels in the vertical to perform data assimilation using past data from 1958 to 1993 (Kalnay and Jenne, 1991; Kalnay et al., 1993). The European Centre for Medium-Range Weather Forecasting (ECMWF) is undertaking a similar reanalysis project with a current version of their model. The idea of a uniformly assimilated data set is attractive and believed important for the study of climate and climate changes. Current archives of grid-point data commonly used in climate studies are derived from operational Numerical Weather Prediction centers, and are the results of production data assimilation suites. As the centers upgrade their analysis or forecast procedures over the years, the character of the model analyses often change, as has been pointed out previously by many scientists. In studies of the climate change to date, researchers have had to deal with changes in the model data due both to real atmospheric changes and due to changes in assimilation procedures. For this reason reanalysis projects were proposed some years ago (Bengtsson and Shukla, 1988) to remove changes due to assimilation procedures as much as possible. It is only recently that these efforts are coming to fruition. Since the resulting analyses will be valuable to the scientific research community for years to come, it is useful to document the character of the data by comparison with actual observations, since the current analysis/forecast procedures are certainly not perfect. In this paper, we analyze the land-surface

and boundary-layer (BL) components of the NMC/NCAR reanalysis system, and point out both the strengths and weaknesses apparent in the data.

The NCAR/NMC reanalysis is the first to be available for 1987, so we compare the surface meteorological parameters and surface energy budget of their T-62 L28 reanalysis (archived every 6-hrs) with data from the 1987 First ISLSCP (International Satellite Land Surface Climatology Project) Field Experiment (FIFE) site in the Konsa prairie south of Manhattan, Kansas. We also explore how well short-term 24-hr forecasts from the 1987 reanalysis, using the same version of the model at a higher T-126 resolution, reproduce the observed diurnal cycle for selected days. During FIFE, an extensive series of surface meteorological observations, radiosondes and surface energy budget measurements were collected during the 1987 summer growing season (Sellers et al., 1988, 1992). The FIFE observations were made on a 15 x 15 km site. Betts et al. (1993) averaged the surface meteorological and flux data to give a single time-series representative of the FIFE site for the time period May 24 to October 16, 1987. They used this data set to identify errors in the ECMWF land-surface and boundary layer (BL) formulations (Betts et al., 1993); subsequently this and other data sets were used to develop improved parameterizations for that model (Viterbo and Beljaars, 1995). This compacted FIFE time series has proved useful for other land surface model development studies (Liang et al., 1994; Chen et al., 1995).

This paper compares this average FIFE time-series with products from the MRF reanalysis model. The model representation of the diurnal and seasonal cycle is encouraging, although the data identify aspects of the model parameterizations that need further development. It is important to realize that we are using an average time series for a 15 x 15 km domain in Kansas to identify

systematic errors in a global model with a considerably larger effective grid resolution of order 100-200 km (depending on the spectral resolution). This disparity of scale is largely offset by the fact that the diurnal cycle over land averages over considerable advection distances (again of order 100 to 200 km). The other reason that the comparison is meaningful is that the central US rawinsonde network is sufficiently dense to define the synoptic-scale fields down to the resolution of the global model. Although the global reanalysis uses the upper air observations (and the surface synoptic data over the ocean), the diurnal cycle of temperature and humidity and the surface fluxes over land are all calculated from the model land-surface parameterizations. By studying both the seasonal cycle, the day and night differences and the diurnal cycle on days with and without rainfall, we will look not for exact detailed agreement between model and observations, but for indications of systematic bias; situations where the model parameterizations do not represent the data in a realistic way. This both gives the user a sense of the quality of the reanalysis, as well as indicates directions for further model improvements in the model land-surface and BL formulations. Many of our conclusions are relevant to the current (June, 1995) MRF model, which is the same model version used for the reanalysis but with the higher T-126 horizontal resolution.

2.1 **FIFE data products used**

Both the raw data and most of our averaged time-series are available on CD-ROM (Strebel et al., 1994). The details of the production of our average data are in the appendix of Betts et al., 1993. The editing of the raw data involved both the use of simple range filters and

extensive manual editing of bad data. There were data from up to ten surface portable automated meteorological (PAM) stations in each 30 min. average. Since the publication of Strebel et al. (1994), this averaged meteorological time-series has been extended to the end of 1987 (Betts et al, 1995), and we use here the average time-series from June to October, 1987. We also averaged the surface flux data (labeled FLUX data on Figures) from 13 selected surface sites, which took measurements during the four intensive field campaigns (IFC's). For the seasonal trends and for one period in late July (between IFC's), we shall use a 2 station average of data from Smith et al. (1992a), who generated a continuous flux time series for the whole summer. This data set was used in Betts and Ball (1995). The upper air data we use was from visually tracked radiosondes (Sugita and Brutsaert, 1990a, b), which were launched roughly every 90 mins on almost all sunny days. This data is available also on Strebel et al. (1994) both as raw data (resolution a few hPa) and interpolated to standard 5 hPa levels. We used the 5 hPa data, whenever we averaged data from different days. The vertical resolution of the sonde data is much finer than the MRF model, so we reduced the sonde data vertical resolution to 20 hPa (by averaging) to give a fairer comparison. We shall show the diurnal rise of the BL for several pairs of days during the season. The MRF sounding data was simply averaged in the model sigma coordinates.

2.2 **Summary of MRF land-surface model**

The current version (June, 1995) of the MRF model utilizes the 2-layer soil model of Mahrt and Pan (1984) and Pan and Mahrt (1987) with minor modification based on Pan (1990). The soil model includes soil thermodynamics and soil hydrology, both modeled as diffusion

processes. The primary feature of the soil model is the use of diffusivity coefficients that are strongly modified by the soil water content. The thickness of the two soil layers in the reanalysis model was 10 and 190 cm. We present the equations for the evaporation model, since this is a key process in the surface energy balance. Evaporation is modeled as three components: direct evaporation from the bare soil surface, transpiration through the leaf stomata, and re-evaporation of precipitation intercepted by the leaf canopy.

2.2.1 **Direct evaporation**

The direct evaporation from the bare soil surface is modeled after Mahrt and Pan(1984). It uses an estimate of the soil water flux at the surface as the evaporative flux (bounded by the potential evaporation (see 2.2.4) when the soil is wet):

$$E_{soil}=(1-\sigma_f)(-D(\Theta)_0(\frac{\partial\Theta}{\partial z})_0-K(\Theta)_0) \qquad (1)$$

where Θ is the volumetric water content, $D(\Theta)$ is the hydraulic diffusivity, $K(\Theta)$ is the soil hydraulic conductivity, and σ_f is the fraction of the grid-area covered by vegetation, which is fixed at 0.7 over the globe. The subscript 0 denotes that the quantity is estimated for the first half layer between the middle of the first (10-cm) soil layer and the surface (where a fixed value of Θ is specified).

2.2.2 **Canopy re-evaporation**

When rain falls to the ground, the leaves first intercept the rain up to a canopy capacity of S(=0.002 m), and the excess drips to the ground. The canopy water then re-evaporates at a fraction of the potential rate (E_p: see section 2.2.4) as:

$$E_c = \sigma_f \left(\frac{C^*}{S}\right)^n E_p \qquad (2)$$

where C* is the amount of canopy water and the factor n is set to 0.5. C* is bounded between zero and S. The interception model is similar to that of Rutter et al. (1971), as described in Pan and Mahrt (1987).

2.2.3 **Transpiration**

This is the process whereby vegetation extracts water from the root-zone and releases it to the atmosphere from the leaf stomata during photosynthesis. The MRF model uses a potential evapotranspiration (E_{tp}: see section 2.2.4), reduced by a soil wetness function and the fraction of the canopy that is dry.

$$E_t = \sigma_f \left(1 - \left(\frac{C^*}{S}\right)^n\right) \overline{\beta_i}\, E_{tp} \qquad (3)$$

The soil wetness reduction factor $\overline{\beta_i}$ (bounded between 0 and 1) is a weighted average for the

first two soil layers (10 and 190 cm deep). For the i^{th} layer β_i is defined as:

$$\beta_i = \frac{\theta_i - \theta_{wilt}}{\theta_{fc} - \theta_{wilt}}. \qquad (4)$$

where θ_{fc} is the field capacity (75% of a saturation value of 0.47), and θ_{wilt} (=0.1) is the wilting point. Only the portion of the canopy that is dry is allowed to transpire.

2.2.4 **Potential evaporation and potential transpiration**

The MRF model differs from many land-surface schemes (Dickinson, 1984, Sellers et al., 1986, Viterbo and Beljaars, 1995) in that it first calculates potential evaporation and potential evapotranspiration, which are then used to compute E_p and E_{tp} in (2) and (3), and to set an upper bound on (1). The potential evaporation is based on a Penman equation (Eq. 5 in Pan, 1990):

$$L\,E_p = \frac{[(1-\alpha)S\downarrow + L\downarrow - \sigma T_a^4 - G]\Delta + (1+\gamma)LE_A}{\Delta + 1 + \gamma} \qquad (5)$$

where $S\downarrow$, $L\downarrow$ are the incoming short-wave and long-wave radiation fluxes, α is the surface albedo (specified at each grid-point), L is the latent heat of evaporation of water, σ is the Stefan-Boltzmann constant (the surface emissivity is 1.0), T_a is a surface temperature corresponding to the potential temperature of the first model sigma level, and G is the ground heat flux. The other terms are defined as follows:

$$\gamma = \frac{4\sigma T_a^3}{\rho_a c_p C_h V} \qquad (6)$$

where ρ_a, C_p are air density and specific heat, C_h is a surface transfer coefficient for heat and V is the surface wind speed. This term comes from the dependence of the outgoing longwave on T_a.

$$LE_A = \rho_a L C_h V (q_s(T_a) - q_a) \qquad (7)$$

where q_s is the saturation mixing ratio, and finally

$$\Delta = \frac{L}{C_p} \frac{dq_s}{dT}\Big|_{T_a} \qquad (8)$$

When vegetation is present, the MRF model also defines a potential evapotranspiration representing evaporation from a plant with no water stress. This uses a fixed minimum stomatal resistance r_s, dependent on vegetation type at each grid point (chosen as the annual minimum from Dorman and Sellers, 1989) to modify the Penman equation (Monteith, 1965), to obtain (Eq. 6 in Pan, 1990):

$$L\,E_{tp} = \frac{[(1-\alpha)S\downarrow + L\downarrow - \sigma T_a^4 - G]\Delta + (1+\gamma)LE_A}{\Delta + (1+\gamma)(1+C_h V r_s)} \qquad (9)$$

Note that r_s in the model has neither seasonal nor diurnal dependence. One consequence is that evapotranspiration is significant in the model at night if LE_A is large, for example in strong winds.

Both (5) and (9) are derived from energy balance concepts. However neither of them represents the actual surface energy balance in the MRF model, nor is T_a the model surface temperature. The model evaporation is calculated from them using (2) and (3), and the total evaporation is then an *input* to the model surface energy balance. This energy balance involves the simultaneous solution of the ground heat flux, the model surface temperature T_{surf}, the longwave radiation field and the sensible heat transfer to the atmosphere, *given the calculated surface evaporation*. Although this method for calculating the surface energy budget appears to be satisfactory most of the time, we shall show examples in June where the limitations of several model parameterizations combine to give an unsatisfactory surface energy budget.

2.2.5 **Surface flux parameterization**

The lowest model layer is assumed to be the surface layer (sigma=0.995) and the Monin-Obukhov similarity profile relationship is applied to obtain the surface stress and sensible and latent heat fluxes. The formulation was based on Miyakoda and Sirutis (1986) and has been modified by P. Long (personal communication) for very stable and very unstable situations. Bulk aerodynamic formulae are used to obtain the fluxes, once the turbulent exchange coefficients have

been obtained. The roughness length over ocean is updated with a Charnock formula after the surface stress has been obtained.

2.3 **Summary of the MRF boundary layer model**

There is no explicit boundary layer parameterization in this version of the MRF model. A local stability dependent diffusion scheme is used for the boundary layer as well as the free atmosphere. This scheme follows Louis (1979) and is quite common among global weather and climate models. The coefficient of diffusivity for momentum (suffix m) and both heat and moisture (suffix h) is expressed in terms of the vertical gradient of the wind as

$$K_{m,h} = l^2 f_{m,h}(Ri) \left| \frac{\partial V}{\partial z} \right| \qquad (10)$$

where the mixing length l is defined as

$$\frac{1}{l} = \frac{1}{\kappa z} + \frac{1}{\lambda_c} \qquad (11)$$

κ is the von Karman constant (=0.4) and λ_c is the asymptotic length scale (=250 m). The stability dependence is built into the function f(Ri) where Ri is the local gradient Richardson number. For momentum diffusion, the stability dependence function is given as

$$f_m = \begin{cases} [1+8(\dfrac{-R_i}{1+1.746R_i^{1/2}}], \ when \ R_i<0 \ (unstable) & (12) \\ [\dfrac{1}{(1+5R_i)^2}], \ when \ R_i \geq 0 \ (stable) & (13) \end{cases}$$

The corresponding function for temperature and humidity is given as

2.4 **Summary of convection model.**

Penetrative convection is simulated following Pan and Wu (1994) based on Arakawa and Schubert (1974), as simplified by Grell (1993). Convection occurs when the cloud work function exceeds a certain threshold. The cloud work function is a function of temperature and moisture in each air column of the model gridpoint. Cloud mass flux is determined using a quasi-equilibrium assumption based on a threshold cloud work function. The temperature and moisture profiles are adjusted towards the equilibrium cloud function within a specified time scale using the deduced mass flux. The major simplification from the original Arakawa-Schubert scheme is to consider only the deepest cloud and not a spectrum of clouds. The cloud model incorporates a downdraft mechanism as well as the evaporation of precipitation. Entrainment into the updraft and detrainment of the downdraft into the sub-cloud layers are included. The scheme as formulated does not detect low level inversions, which might inhibit deep convection (see 3.2.1 later).

3. **Results**

We show a series of different comparisons between the FIFE data and a nearby grid point of the NMC/NCAR reanalysis using the MRF model. First we compare the seasonal cycle of the surface energy budget from the 6-hr surface flux averages in the reanalysis archive. Then we shall compare the surface daytime diurnal cycle over the season, using the 6-hr values from the same archive. After this we short-term (24-hr and one 48-hr) forecasts from the reanalysis (with the same model at a higher spatial resolution of T-126) to show in more detail how well the model reproduces the observed diurnal cycle for the surface and BL for selected days in June, July, August and October, 1987.

3.1 **Seasonal Comparison with the FIFE data**

This comparison uses the reanalysis archive of 6-hourly mean surface fluxes and surface meteorological data every 6 hours.

3.1.1 **Surface flux comparison**

We first combine 4 of the 6-hr surface flux averages to give the daily average, and compare this day-averaged data with the FIFE data.

Figure 1 shows incoming solar radiation ($S\downarrow$ in W m^{-2}) from the FIFE PAM data and

precipitation (in mm d^{-1}) for the five-months from June to October (Julian Day 152 to 304). The dotted curves are the model, while the solid curves are the data. The general agreement is fairly good, showing the pattern of rainy days and dry periods. The highest model values for incoming solar radiation exceed these observed during dry periods (e.g. 202-212 in late July), suggesting the model atmosphere is too transparent. On rainy days, the observed minima are generally also lower, suggesting that cloudiness is underestimated in the model. This excess incoming energy is partly offset in the surface energy budget, because the model albedo at this grid point is 24%, while that for the data is somewhat lower (18-21%; see Betts et al. 1993). The model shows most of the major precipitation episodes (recall that the data is a much smaller domain than the model grid square), but the distribution shows some differences. The model has much more precipitation in June and early July; less in August, and October than was observed (and a little more in September, which was a dry month). This will have some impact on the time sequence of evaporation in the model. The excess precipitation in June and early July appears to be linked to a deficiency in the model surface diurnal cycle caused by feedbacks between several model parameterizations (see section 3.2). The total 5-mo precipitation in the model is 495 mm, a little more than the 410 mm observed at the FIFE site. The diurnal distribution of precipitation is also different (not shown): 72% of the model precipitation falls in the daytime hours (12-24 UTC), whereas 57% is observed to fall at night. The model often rains in the morning before local noon (see 3.2.1); this is rarely observed.

Figure 2 shows net radiation (RNet) and ground heat flux (plotted as -G). The dotted lines are again the reanalysis; while the solid lines are now from the Smith data. The dashed RNet line is an average of the PAM net radiometers. The model ground flux is generally less than the data

in June and July. The difference between the solid and dashed RNet curves is an indication of calibration uncertainties in the net radiation data (Smith et al., 1992b), which change sign during the season. Comparing model and data, the net radiation differences are less than the differences in $S\downarrow$ in Fig 1, both because the model albedo is greater, and the model net longwave bias (not shown) is upward relative to the data. In September, the model net radiation is less than observed. Figure 3 compares the sum of sensible and latent heat (SH+LH) from model and data; these balance RNet-G in Fig 2 (the Smith data ends on October 16). Averaged over the whole period they agree closely, although there are periods when the model and data differ by ±15 W m^{-2}. The total surface energy flux in the reanalysis is generally less than the data in September and October. Figure 4 shows separately SH (lower curves) and LH (upper curves). Although there is some agreement, particularly in long-term means, the model generally swings between larger extremes, with a time frequency of several days. Since SH and LH compensate, we see in the reanalysis matching pairs of high evaporation and large negative heat flux in some 24-hr averages. There are also occasions where the model SH flux exceeds any values observed in the summer.

These differences can be understood more easily from separate day and night comparisons, because the behavior of the MRF reanalysis model is significantly different day and night. The 12-hr averages (0-12 and 12-24 UTC), correspond closely for the FIFE area to night and day-time averages (local noon is 1820 UTC). The middle section of Figure 5 shows the night-time SH and LH fluxes; below we show the 24-hr precipitation and at the top the night-time wind speed (as -V) at 6 UTC. The solid SH and LH curves with little variation are the data, and the dotted curves with large extremes are from the reanalysis. There are nights with a mean

evaporation of 150 W $m^{-2,}$ and a corresponding large downward sensible heat flux. For most nights, the reanalysis fluxes are larger in magnitude than the observations. An important part of the reason for this is that the model does not explicitly switch off evapotranspiration at night. The extreme values appear to be on nights of higher wind. The transfer coefficients in this stable regime may also be too large in high winds. Mst of the extremes seen in Figure 4 for the diurnal averages come from these extremes at night.

Figure 6 compares the daytime LH and SH (sign reversed) together with the 24-hr precipitation. The ranges in model and data are now much more comparable. During the daytime, the larger extremes in the reanalysis follow precipitation episodes. Figure 7 shows the daytime mean surface Bowen Ratio below and the daily precipitation at the top. During non-rainy periods, the reanalysis often has a higher BR flux than the observations. The larger fluctuations in the model now become more visible. The rise and fall of Bowen Ratio in the model after rainfall are generally more extreme than observed. We see that in August and September the model often has a daytime mean $BR \geq 1$, that is higher than the value reached in the data in early August at the end of an extended dry period. The highest model values around day 222 (August 10) can in part be explained by there being no significant rain in the reanalysis on August 4 (day 216). However the larger reanalysis Bowen ratios around day 195, day 230, and day 265, which are shortly after significant rain in the reanalysis, suggest that improvements may be possible in the coupling of the vegetative resistances to the soil moisture, or perhaps that rainfall does not diffuse quickly enough into the deep soil moisture reservoir.

In a climatic sense the seasonal cycle of the surface fluxes in the MRF reanalysis (from May to October in Figure 7) are quite good. We see though some significant differences between

model and data, and between the day-time and night-time behavior of the model. We will explore these differences further in sections 3.2 and 3.3 using short-term forecasts from the reanalysis to look at the diurnal cycle. First however we will compare the seasonal behavior of the surface diurnal cycle.

3.1.2 **Diurnal cycle in reanalysis**

The reanalysis archive has near-surface atmospheric parameters every 6 hr, calculated from a 6-hr forecast from the standard synoptic times of 00, 06, 12 and 18 UTC. Figure 8 shows the comparison of the monthly mean surface diurnal cycle of potential temperature, θ, against mixing ratio, q, compared with the same average from the FIFE data (solid lines). We show only three values at 12, 18 and 24 UTC, joined by lines. In each case the lowest θ value is at 12 UTC. These represent quite well the daytime diurnal cycle, as they correspond roughly to local solar times of 6, 12, and 18. The data is shown solid and the reanalysis dashed. The dashed lines marked 970 (approximately the surface pressure) and 800 correspond to saturation at these pressures (in hPa), so that the daytime rise of saturation level or lifting condensation level (LCL) can be seen. The agreement in July, August, September and October is good for the monthly mean diurnal cycle. Typically the model is slightly moister than the data. In June however the reanalysis has a much moister (and cooler) mean diurnal cycle. The morning rise of q in the model is 5 g Kg^{-1}, instead of 1 g Kg^{-1} in the data, a huge difference. We saw in Figure 1 that precipitation in June was higher in the reanalysis than observed. The different diurnal behavior appears to be linked to this (see section 3.2).

Figure 9 shows the monthly mean θ_E and P_{LCL} (the pressure height of the LCL; an estimate of cloud base) at 18 UTC (near local noon) for the reanalysis (dashed) and data (solid). Generally the reanalysis is about 2 K higher in θ_E and 20 hPa lower in P_{LCL} but in June this θ_E bias exceeds 10 K. In June, the near surface air in the model is also much closer to saturation. At noon P_{LCL} is only 50 hPa above the surface, whereas P_{LCL}=120 hPa in the data (as can be also seen in Figure 8). These model differences in June are clearly significant in terms of the feedback between surface and convection, and are examined in the next section. Figure 10 compares two averages of the diurnal cycle of the surface wind. In Summer (June, July and August), the observed wind speed (at 5.4 m) is uniformly stronger than the model (for 10 m). In Fall (September and October) the observations have a stronger diurnal cycle, while the model diurnal cycle is weaker.

3.2 **Model behavior in June**

Because the reanalysis has excessive daytime rain in June and correspondingly high noon values of θ_E, we looked more closely at the possible surface interactions responsible in the model. There are many days in the middle of June (and some in early July), when it rained during the daytime in the reanalysis, and the daytime diurnal cycle was quite unlike any days that were observed. On these days (June 9-15 and 18-23, July 4-5 and 8-9 are examples), the air near the surface remained nearly saturated in the morning after sunrise. On many days, the relative humidity stayed above 90% all day.

3.2.1 **Mid-June morning rainfall anomaly**

For the period June 11-15 there was no rain at all at the FIFE site; while at the model gridpoint there was rain during the daytime period on each day. For the subsequent similar period of June 18-23, again there is rain at the model gridpoint during the daytime on each day. On three days (June 18, 20, and 22), it rained at the FIFE site in the early afternoon, while on June 19, 21 and 23, it did not rain. Figure 11 contrasts the daytime diurnal cycle from 12 to 24 UTC for 3 averages. The squares mark the diurnal cycle for the average of the group of 3 "dry" FIFE days, with the typical diurnal cycle in which θ_E rises to around 350 K and saturation pressure lifts to 820 hPa (the pressure of the LCL) in the afternoon. The data are hourly averages from 12 to 24 UTC. The circles are the average of the three days with early afternoon rain. Here we see θ_E rise faster in the morning hours reaching 355 K at 1800 UTC (near local noon). Rain follows, and there is a sharp fall of both θ_E and LCL with the rain. This is associated with evaporation driven downdrafts bringing low θ_E air to the surface (see, for example Betts, 1976, 1984). In sharp contrast, the 6-day average (dotted) from the reanalysis (for which all days were very similar), shows near-saturation at the surface all day. θ_E rises above 360 K by 1800 UTC. On all days it rains morning and afternoon. For the earlier period June 12-15, the model behaves similarly, but by 18 UTC the surface reaches an even higher $\theta_E \approx 380$ K and a mixing ratio of 24.5 g Kg^{-1} (not shown). It is clear that the coupling between the surface fluxes, precipitation and the surface diurnal cycle is quite different in the MRF reanalysis model than is observed. One obvious reason from Figure 11 is that the model may not adequately represent unsaturated convective downdrafts, which sharply end the rise of θ_E once it rains. The model uses a modified Arakawa-

Schubert parameterization for convection, discussed briefly in Section 2.4. However there is the more fundamental question of why it rains in the model soon after sunrise.

To explore this more closely, we ran a 48-hr forecast from 12 UTC on June 20. We found several possible causes contributing to the unrealistic model behavior. Figure 12 shows the 48-hr forecast of model rainfall, model available energy (RNet-G), computed potential evaporation (E_p), surface SH and LH fluxes, as well as the three components of the LH flux from the soil (E_{soil}), evapotranspiration (E_t) and direct evaporation off the wet canopy (E_c). The SH flux is small and the LH flux is close to the potential evaporation. The largest contribution comes from evaporation off the wet canopy, and the second largest is from the wet soil. Evapotranspiration is small because the canopy is wet. Even though the model atmosphere is close to saturated at the surface, evaporation continues at the potential rate from the wet surfaces. Figure 12 shows that one problem contributing to the rainfall in the delayed cloud radiation feedback. The short-wave calculation is only updated every 3 hrs. The rain starts in the model at forecast hour 3 (1500 UTC) and from 3-6 hrs it rains about 1 mm hr^{-1}: this keeps the surface wet. (RNet-G) remains very high during this period (reaching 600 Wm^{-2} at 6 hrs just before local solar noon), because the incoming shortwave does not see the precipitating clouds until the next radiation update. This drives the large surface evaporation. At 6 hrs, the short-wave scheme 'sees' the clouds, (RNet-G) falls 250 Wm^{-2}, θ_E falls 3 K at the surface, and the rain stops for the next 2 hrs. Something similar happens on the next day. More frequent updates of the cloud fraction in the radiation scheme would reduce this on and off behavior. The 250 Wm^{-2} fall in RNET with precipitation in the model is also only half that observed, if we compare the afternoon RNet values for the dry and wet averages in Figure 11 (not shown).

Figure 13 shows the model profiles of θ_E and θ_{ES} against pressure for the time-period spanning the morning rain on the second forecast day (June 21). These show that the formulation of the convection scheme is also playing some role in permitting rain. The vertical dashed lines are drawn through the surface θ_E for the three times. Even though there is an inversion with a θ_{ES} maximum near 850 hPa, rain starts at 27 hrs (15 UTC on June 21).This is unrealistic. The convection scheme, as formulated, does not see this inversion, which therefore plays no role in restricting deep convection. Once rain starts, the inversion itself warms steadily with the convective heating, and the surface θ_E continues to rise, driven by the surface evaporation into a shallow layer.

The key reason however why the model surface diurnal cycle does not resemble the data is that the surface fluxes in the model are not mixed through a deep layer. Figure 13 shows that the model "mixed" layer (up to the first θ_{ES} minimum) is barely 20 hPa deep, whereas on this day in FIFE, the mixed layer grew to 120 hPa in depth by local noon (not shown). With potential evaporation, a nearly saturated surface, and little vertical mixing, the local change at the surface (on a (θ,q) diagram) is indeed a vector nearly parallel to the surface pressure as seen on Fig 11 (see Betts, 1994). With no vertical BL development, all the surface θ_E flux goes into a shallow layer and θ_E increases, maintaining precipitating convection.

The model lacks several key negative feedbacks. The incoming net radiation responds only every three hours to clouds. The convection scheme can produce precipitation even in the presence of a BL inversion, and it does not reduce BL θ_E through downdrafts. Vertical mixing in the model is limited by the downgradient BL diffusion scheme. The model formulation of potential evaporation is also suspect. This formulation was originally introduced in the MRF

model to reduce evaporation from the bucket model (Pan, 1990) in dry atmospheric conditions. In June 1987 in the reanalysis, surface conditions are near saturation. Evaporation in the model stays close to the potential rate (which is of order 300 W m^{-2} for a daytime average in mid-June), even when the relative humidity stays near 100% in the morning hours. It is not clear that the evaporation, surface wind speeds (which are low on June 20-21) and the thermodynamic structure near the surface are all consistent. This needs further investigation. The FIFE data show that as the surface and BL warm and moisten after sunrise, cloud-base always lifts as drier air is mixed down from above (Betts and Ball, 1995). In the MRF model (which has little vertical mixing), in these wet surface conditions, the surface stays cool and saturated, and a large latent heat flux modifies only a shallow layer, producing high values of θ_E, which trigger precipitation and the feedbacks we have seen.

3.2.2 **Late June diurnal cycle**

In late June, there was a break in the pattern of morning rain in the reanalysis. We compare in Figure 14, the surface energy balance for a 2-day average, June 26 and 27, (which were similar dry days in FIFE), using 24-hr forecasts starting at 12 UTC from the reanalysis, again with the same MRF model at T-126 resolution. In descending order the pairs of curves are RNet, LH, SH and G (sign reversed) fluxes with the FIFE FLUX data solid and the MRF reanalysis dotted. The agreement is good considering the and fluctuations in cloud cover in both the data and model. The ground flux is less peaked in the model than the data. The fall of SH and rise of LH near forecast hour 5 (17 UTC) in the model is associated with a very brief shower in the

model on June 27. Figures 15a and 15b compare the BL evolution for model (dashed) and data (solid) for the 2-day average. By afternoon the model has produced a nearly well-mixed layer. However, although the surface fluxes are modeled quite closely, we see that the model BL is shallower by about 40 hPa in the afternoon. The model has a noticeably less well mixed structure in mixing ratio (q) than the data, and a slightly weaker surface superadiabatic layer. Figure 16 compares the surface daytime diurnal cycle of θ and q. Lines corresponding to saturation at the surface pressure (980 hPa) and 800 hPa, and θ_E=330, 340 K are shown dashed. The model forecasts the diurnal rise of θ well, but the model is considerably moister than the data at the surface throughout the day. The data are plotted hourly from 1215 to 2315 UTC for both the FIFE 2-day mean and the MRF mean. The small numbers denote the hours. The poor vertical mixing of q shown in Figure 15b, the extra rain in June, and generally higher LH fluxes at night are probably all linked to these higher mixing ratios near the surface. The model surface starts near saturation at the surface pressure of 980 hPa at 1215 UTC, and cloud base rises more slowly than in the data, presumably because of the reduced vertical mixing in the model. Similarly the model θ_E remains a few K higher than the data throughout most of the day.

3.2.3 **Summary of model behavior in June**

In June, several features of the model appear to interact to produce excessive daytime rain in the reanalysis. High ("potential") evaporation into a shallow layer with too little vertical mixing produce a near saturated condition with high θ_E. This triggers the precipitation in the convection scheme (which does not see the BL inversion). The clouds are not seen by the radiation scheme

for several hours, so the surface net radiation is not reduced quickly by clouds. The convection scheme, unlike precipitating convection is the atmosphere, does not reduce BL θ_E, so the model lacks negative feedbacks to reduce the rise of θ_E near the surface. However by late June, when the atmosphere is drier, this anomalous model rain disappears. In late June the model behavior is then quite realistic, although the BL growth is somewhat less than observed. The excess day-time rain reappears again in early July, and then finally disappears for the summer, probably because the soil dries out during an extended dry period. Many of the details of these model feedbacks are still being investigated further; and no doubt will lead to improvements in the model parameterizations.

3.3 **Mid-Summer diurnal cycle**

After July 9 (Julian day 190) the excess daytime model rainfall, discussed in the previous section, appears to disappear at the FIFE gridpoint. As observed, the rest of July had little precipitation, soil moisture falls in the model, and the model surface BR rises (Figure 7). We now present some comparisons from this period.

3.3.1 **Late July dry period**

July 30 and 31 were two days were towards the end of an extended dry period of 2 weeks without rain. Observed surface BR's reached their highest values of the summer (Kim and Verma, 1990), as did observed air temperature T and surface temperature, T_{surf}. Again we ran 24-hr

forecasts from the 12 UTC reanalysis for each day, and averaged the two to show a mean diurnal cycle. Figure 17 compares the daytime diurnal cycle for model and data. The shape of the diurnal cycle is very similar, although an offset is visible. The model is cooler and for most of the daytime moister than the data. Both model and data reach $\theta_E \approx 352$ K, but the data has a higher P_{LCL} throughout the day by 30-40 hPa. Figure 18 shows the difference $\Delta T = T_{surf} - T$. For the data, T_{surf} is a radiometric temperature. In the dry conditions of late July, ΔT actually exceeds 7 K at solar noon. In the model however this difference barely exceeds 1 K. At night the observed ΔT is again larger in magnitude. The model surface temperature appears to be too tightly coupled to T at 2 m. This appears to be a general characteristic of the model. Improvements may be possible in the model surface layer parameterization. The model has the same roughness length for heat (Z_{0h}) and momentum (Z_{0m}). One study using the FIFE aircraft data (Betts and Beljaars, 1993) gave $(Z_{0m})/(Z_{0h})$ of order 20. Other studies have suggested that this ratio can be even higher (e.g. Beljaars and Holtslag, 1991). Increasing $(Z_{0m})/(Z_{0h})$ increases the skin-air temperature difference. The model generates a deep afternoon BL to about 820 hPa (not shown). There is no sounding data for these two days for comparison.

Figure 19 shows the comparison between the model and the Smith flux data (the 13-station average is not available in late July). The RNet values are quite close. In the afternoon, the model BR (SH/LH) is lower than the observations. Although these observations are based on only 2 BR stations from Smith et al. (1992a), Kim and Verma (1990) show a still higher afternoon BR of 1.3 at another FIFE site on July 30. At night the same pattern is seen (as in Figure 5) of higher LH and downward SH fluxes in the model. The lower model BR in the daytime in late July and greater model evaporation at night are probably responsible for the cool moist shift of the diurnal

curve of the model from the data, seen in Figure 17. It appears that the model evaporation is higher than the observations towards the end of this dry period. The model 2 m deep storage reservoir for soil moisture appears to be more than adequate to maintain the surface evaporation for three weeks without rain. However by August 9-10, the model BR has climbed steeply (Julian day 221-222 in Figure 7), while the observed BR of 0.8 is similar to that in late July. Rain fell on August 4th, and 8th: but there was almost none in the reanalysis for these dates (see Fig 1); so that the soil moisture continued to fall steadily in the model between July 30 and August 10 (days 211 to 222 in Figure 23 later). Consequently the model BR continued to climb from August 1 to 10.

3.3.2 **9-Day August Average**

We averaged the diurnal cycle of 9 selected days in August from the FIFE 1987 data and the MRF reanalysis to show a "representative" mid-summer behavior of the model. There is extensive field data for these days. 24-hr forecasts were run starting from 12 UTC on August 6 (Julian Day 218), 7, 9, 10, 15, 16, 17, 20, and 21. These days had little daytime rain in FIFE, and no daytime rain in the reanalysis. Figure 20 shows the comparison of net radiation and ground heat flux. The agreement in RNet is excellent, well within the measurement uncertainties (the range in the data represent different measurement systems and calibration factors: see Smith et al., 1992b). The highest (long dash curve) is the Smith data which has a higher calibration than the curves labeled PAM and FLUX (from averages of these stations). The model curve lies within the envelope of the data during the daytime, but the model has higher outgoing values at night. This is

due in part to the higher surface temperatures at night (not shown). The mean ground heat flux is quite close in model and data (the Smith data, an average of only 2 sites, has the higher ground flux), although the daytime model ground flux profile is flatter.

Figure 21 shows the comparison of mean SH and LH fluxes at the surface. The 13-station flux average are the solid pair of data curves; the two station Smith average (which are slightly higher) are shown long-dashed: they agree well. We consider the 13-station average to be the most representative, and will present it whenever it is available. The model (short dashes) has a higher daytime SH flux and lower LH flux, giving a higher daytime Bowen Ratio (BR) near solar noon. However the pattern reverses by sunset and at night. The model evaporation stays high, and the energy is supplied by a larger downward sensible heat flux in the model than the data. This is the same as the night-time behavior we saw in the seasonal data in Figure 5. In fact this group of 9 days includes several of the extreme peaks on Figure 5, such as day 228. These comparatively large model surface fluxes at night are associated with transfer coefficients that are high for this stable regime, as well as non-zero evapotranspiration at night in the model. We will look at specific cases in the next section.

Shifting to the mean daytime (1215-2315 UTC) surface thermodynamic cycle, Figure 22 shows the (θ,q) comparison. The agreement is encouraging. The model shows a slightly larger rise of θ than the data. At the afternoon θ maximum, the model is a little warmer (by$\approx$1 K) and drier, with a higher saturation level. The small daytime rise and fall of q in the model is quite realistic: the more complex structure in the data may be partly meteorological "noise". The model behavior is consistent with its larger surface SH flux and smaller LH flux (Figure 21).

Although the model 2-m temperature follows the data quite well, the surface temperature

in the model does not get as warm in the day, nor cool as fast at night: the model behavior is very similar to that seen in Figure 18. One consequence is that the model outgoing longwave radiation is too large at night (not shown).

3.3.3 **August before and after heavy rain**

While the 9-day August mean suggests that model *averages* in mid-summer may be quite good, the individual days show that the model tends to greater extremes as suggested by Figure 7. There was a major rain event on August 12-13 (Julian day 224-225). Figure 23 shows soil moisture (SM) at 18 UTC for the two model layers for the individual days for which we made 24-hr forecasts. Soil moisture is low in the model on August 9 and 10 before this rain, and then declines from a peak in the period August 15-21 after the heavy rain event. Note that not much of the heavy rain that fell reaches the second soil layer so that the deep soil reservoir is not replenished. We compared an average of the forecasts from 12 UTC on August 9 and 10 (which were similar days before the heavy rain) with August 15 afterwards.

Figure 24 shows the day-time BR for the model and the FLUX data for these before and after rain cases. The net radiation curves are similar for model and data (not shown). Following the rain, the observed daytime BR does fall significantly from values around 0.8 to 0.35 (solid lines). However the fall in the model (dotted lines) is much more extreme from around 1.8 to near zero.

Figure 25 shows the SH flux for the whole 24-hr period. During the daytime, with the dry to wet transition, the model peak SH flux drops from 340 Wm^{-2} to zero, in comparison with the

smaller fall in the data from 240 to 120 Wm^{-2}. The difference at night shows (to a greater extent) the same behavior seen in the August mean in Figure 21. The observed downward SH flux is larger on August 15 than August 9-10, but in both cases the downward SH flux is larger in the model than the data. Figure 26 shows the corresponding differences in LH flux. As expected from Figures 24 and 25, the model shows a much greater daytime increase in evaporation after the rain than the data. At night, Figure 26 shows that the very large downward sensible heat flux of ~150 Wm^{-2}, seen in Figure 25, is balanced by a comparably large evaporation term. These high night-time fluxes correspond to the spike seen in Figure 5 for day 228. Figure 27 shows the model surface transfer coefficients for heat and moisture (C_h) and momentum (C_d). On August 9 and 10, there is a large diurnal range, but on August 15, the diurnal range is non-existent (the surface daytime superadiabatic layer is absent: see later) and the night-time transfer coefficient is high. Figure 28 shows the surface wind speeds. August 15 is a day with stronger winds, but the model winds at 10 m are still not quite as strong as the winds observed at 5.4 m. As we suggested in 3.1.1 in the discussion following Figure 5, it appears that the model surface transfer coefficients are too large in higher winds; in particular this drives too large fluxes at night. The night of August 15-16 is a good illustration of this. However, a major part of this error is that the model does not explicitly switch off evapotranspiration at night. For this night with high winds about half the evaporation is evapotranspiration. On this day, there is too much daytime evaporation as well with a stable surface layer and moderately strong winds. Figure 29 shows the surface-air temperature difference (ΔT). Although both model and data show a fall of ΔT after the rain, the model diurnal range is much smaller both in the daytime and at night, as seen earlier in Figure 18 for late July. As we noted before, this is probably a consequence of having the same roughness

lengths for heat and momentum in the model. Figure 30 compares the daytime diurnal cycle of θ and q for the two cases. For August 9-10, the model is a little drier, presumably because the model surface BR is higher (Figure 24) but both model and data reach a similar afternoon state. It appears that reduced BL entrainment of warm, dry air and the higher surface BR in the model appear to compensate. For August 15, the surface diurnal curves of model and data are very different. The model is cooler by about 2°C throughout the day (and the following night: not shown). Although the diurnal patterns are quite different, remarkably the daytime rise of temperature in the model is 10°C, similar to that observed. How can this be, given zero surface SH Flux (Figure 25)? Horizontal advection may be partly responsible, but the major contribution is a downward eddy transfer of heat of order 80 Wm^{-2} at 900 hPa. Similarly there is an upward eddy transport of moisture of order 400 Wm^{-2} near the surface.

Figures 31 and 32 compares the BL potential temperature (θ) against pressure for these two cases. The observations in Figures 31a and 31b (heavy lines) show that August 9-10 had a deep mixed layer (ML) with a top near 800 hPa. The data has again been averaged in 20 hPa layers to give a resolution comparable to the model. We have selected 4 sounding pairs from the 8 that were launched on each day. The model reproduces the time evolution rather well for θ, but the model ML is noticeably shallower by 30-40 hPa in the afternoon, as in the June 26-27 comparison shown earlier (Figure 15). The q profiles in Figure 31b shows a similar shallower BL in the model. Again the reason is the lack of BL-top entrainment in the model. August 15 is a day on which there was a much shallower BL shown in Figures 32a and 32b. The data shows a nearly well mixed BL with a top around 900 hPa (fluctuating about ±15 hPa during the day: there are 4 other soundings not shown). By mid-morning, a weak surface superadiabatic layer is generally

present (the sonde surface data shown is cooler than the other surface meteorological data). In contrast the model has a stable BL structure all day, consistent with the near-zero SH flux shown in Figure 25. The model BL stays cooler than the observations all day. The difference between model and data is also striking in the q profiles in Figure 32b. The model has quite a uniform decrease of q with height, while the observed q gradient in the "mixed layer" (900-960 hPa) is much less. We can again ask how the model θ warms with time, while q remains nearly constant despite a zero surface SH flux and large LH flux. The eddy transport scheme is transporting heat downwards and moisture upwards as mentioned above. The BL wind speeds are quite high on August 15. Figure 33 shows a morning low level jet approaching 20 ms^{-1} in the data and 16 ms^{-1} in the model. Shear driven turbulence must play a significant role on this day, but the stable transports in the model appear to be rather high in the BL as well as at the surface. They must be partly responsible for the near zero daytime BR in the model. Note the compensation of different processes in the model. On August 9-10, less BL-top entrainment of warm dry air, but a larger surface Bowen Ratio appear to largely compensate, so that the daytime rise of θ and small fall of q are similar. Almost the reverse happens on August 15. The model surface BR is too low, but this appears offset by the downward transports of warm dry air. In both cases we see differences in BL structure.

3.3.4 **Summary of mid-summer behavior**

The surface energy budget and diurnal cycle in the reanalysis appears to be much better in mid-summer than in the June period. The model describes well the dry-down following no

precipitation in late July. Perhaps surprisingly it maintains a higher surface evaporation than observed. This may be a consequence of the extra rain earlier, stored as soil moisture in the deep 2 m reservoir. We show a 9-day average in August. In this model and data agree quite well. However we note that averages do hide the fact that the model has greater extremes than the data. The comparison before and after the major rain of August 12-13 shows this clearly. The surface BR falls much further in the model than the data. Generally the model BL is shallower than observed, because the model does not simulate well the entrainment of warm dry air at BL-top. On August 15, a windy day after rain, the model transfer coefficients at the surface and in the stable BL appear to be high both day and night. At night this leads to large evaporation and downward SH flux, in the daytime to large evaporation with near zero SH flux.

3.4 **October comparison**

Figure 34 shows the daytime diurnal cycle for averages of October 7 and 8, both sunny days after the first hard frost on October 1. We show points at 1245 UTC (the morning temperature minimum) and then hourly values from 1315-2315 UTC. As in late July, the model is systematically a little cooler than the data, but the low mixing ratio in October is modeled closely. Figure 35 shows the surface fluxes, the sequence from top to bottom is now RNET, SH, LH, -G with the model dashed and the FLUX data solid. RNET is significantly higher in the model. Some of this is the low model T_{surf}, which reduces outgoing LW, but there is a significant difference of 60 W m^{-2} in the net incoming solar radiation at local noon. As in Figure 1, this suggests that the model atmosphere is too transparent or has too little cloudiness. Betts et al (1993) saw a very

similar difference between the ECMWF model and these observations. The albedo of the FIFE grassland has increased by 2-3% in the fall after the vegetation has largely died : this increases the reflected solar radiation by ≥ 20 Wm^{-2}. However, the model has a fixed albedo of 24%, which is higher than the observed range (see section 3.1.1). In comparison with the observations, the model in October has almost double the day-time LH flux, a larger day-time ground heat flux and a slightly lower SH flux. The observed BR rises steeply in October after the vegetation has largely died and the temperature falls. The model captures only some of this response (Figure 7) since it has a fixed minimum vegetative resistance at each grid-point. The model BL deepens to about 860 hPa during the day, not quite as deep as observed (not shown). The BL mixing ratio increases in the model during the day as observed (not shown). Overall the model handles the seasonal transition to reduced evaporation in the fall reasonably. The observed transition following the first hard frost may be faster than the transition seen in the model, but this can be regarded as a consequence of the fixed minimum vegetative resistance at each grid-point in the model.

4. **Discussion and Conclusions**

The surface fluxes and BL variables feed back in summer through deep convection on the tropospheric temperature, so their accurate simulation is important in a global model. The long time-series data set from the FIFE experiment has again proved of great use in assessing the quality of a global forecast model, through the comparison of the model simulation for a nearby gridpoint. Since the model used in the reanalysis is also the current (June, 1995) global forecast model at NMC, our conclusions are relevant to both the reanalysis and the representation of the

land-surface in summer in current MRF forecasts.

In a climatic sense the seasonal cycle of the day-averaged surface fluxes in the MRF reanalysis are quite good. The comparison of the diurnal cycle of the MRF reanalysis over the seasonal cycle with the 1987 FIFE in Kansas is also encouraging. The model generally reproduces the diurnal cycle of the surface and BL θ, and q to about $\pm 2°C$ and ± 2 g Kg^{-1}. Such close agreement reflects improvements in the model land surface parameterizations in recent years. Figs 36 and 37 illustrate this with a snapshot of the season based on 3 pairs of days in June, July and October. The seasonal rise of SH flux in the model (dotted in Fig 36) as the model soil dries and the air temperature falls, follows the data, even though the model does not have an explicit seasonal vegetation cycle. The diurnal rise of the model 2-m air temperature shown in Figure 37 is within 2 K of the seasonal cycle seen in the data, although the model has a tendency to be cool.

We saw in previous sections some significant differences between model and data, which suggest areas where future model improvements are possible. During the daytime, the fluctuations in surface BR in the model following precipitation events are larger in the model than in the data. We also saw big differences between the day-time and night-time behavior of the model. The surface fluxes at night (evaporation and downward SH flux) are generally too large; they can approach 200 Wm^{-2} , when wind speeds are strong. Short-term forecasts from the reanalysis confirm these discrepancies. The model (downward) sensible and (upward) latent heat fluxes at the surface are generally too large at night (often by a factor of 2 or more), because the transfer coefficients in this stable regime are also correspondingly large, and the model does not explicitly switch off evapotranspiration at night which can be large if the wind speed is high. The impact of these day-night differences in the model is not fully clear from these 24-hr forecasts. It

may be more significant in longer term forecasts, where the integrated budget over the whole diurnal cycle is important. We suggest caution in using the diurnally average surface energy budget of the reanalysis for climate studies, until this is explored further.

One key to an acceptable land-surface scheme is accuracy in the prediction of surface evapotranspiration. In general the MRF model does fairly well in modeling the seasonal fall of evapotranspiration from late June through August to October. The 2 m deep soil moisture reservoir used in the reanalysis probably has more than enough seasonal storage capacity, although there are some indications that it is not properly recharged by rainfall. Perhaps more than two soil layers are desirable. The period in August, however, which we have presented in more detail does show that natural grassland has greater stability than the model simulation. About 80 mm of rain fell between August 10 and 15, and the observed surface BR fell from 0.9 to 0.35 near local noon. The corresponding model BR however fell much more from 1.8 to near zero. Throughout this August 6 to 21 time period, the observed noon BR's are clustered in a narrower range than those of the model. On August 15, a windy day with high soil moisture, the surface fluxes in the model remained high on both day and night despite a stable BL. The model surface transfer coefficients were high and had no diurnal cycle.

Boundary layer depth is generally under predicted in the MRF model, because the down gradient diffusion scheme (Louis, 1979) does not properly represent entrainment at BL-top. Analyses of the FIFE data have suggested that BL entrainment plays an important role (Betts, 1992; Betts and Ball, 1994). However the model sometimes compensates for this by a stable diffusion process. On one day (August 15) when winds were strong, the model diffusion was sufficient to transport heat downwards and moisture upwards, even in the absence of a surface

sensible heat flux. A new BL scheme is under development.

The incoming solar radiation appears to be overestimated in the model, but this is partly offset at the FIFE site by a higher assumed albedo. The reduction of incoming solar radiation by cloud cover is generally underestimated. The update of clouds in the radiation scheme only every 3 hrs produces significant errors in the surface energy budget, when it first starts to rain. In June and early July there is too much daytime rain in the model. This appears to involve the interaction of several components of the surface, BL and convection schemes, and is being investigated further. Too little vertical mixing means the surface θ_E rises too quickly after sunrise in a shallow nearly saturated BL. The convection scheme, which does not see the BL inversion, often produces precipitation which wets the surface. Evaporation stays high as the incoming solar radiation is not reduced by the cloud fields until the next radiation scheme update. The surface stays wet and nearly saturated at high θ_E and light rain of order 1 mm hr^{-1} persists.

The difference between skin temperature and air temperature is always underestimated in the model in comparison with the data, often by several degrees. In the driest part of the summer the measured radiometric surface temperatures were 8 K higher than the model surface temperature. The reverse is true at night, when the observed radiometric surface temperatures generally fall below the model surface temperature. The implication is that the near-surface heat transfer coefficients for heat are in some sense too high in the model for both stable and unstable regimes. At present the model uses the same roughness length for heat and momentum.

The overall seasonal cycle of the land surface interaction in the reanalysis compares quite well with the FIFE data near Manhattan, Kansas. Not surprisingly however, we have found several areas where improvements in the model parameterizations are desirable, and may well lead

to improved medium-range forecasts.

Acknowledgments.

Alan Betts acknowledges support from the National Science Foundation under Grant ATM-9505018, the National Oceanographic and Atmospheric Administration under Grant NA56GP0380, and NASA under Contract NAS5-32356 for the processing of the FIFE data.

References.

Arakawa, A., and W. H. Schubert: 1974: Interaction of a cumulus cloud ensemble with the large-scale environment. *J. Atmos. Sci.*, **31**, 674-701.

Beljaars, A.C.M., and A.A.M. Holtslag, 1991: Flux parameterization over land surfaces for atmospheric models. *J. Appl. Meteor.*, **30**, 327-341.

Bengtsson, L. and J. Shukla, 1988: Integration of space and in-situ observations to study global climate change. *Bull. Amer. Meteor. Soc.*, **69**, 1130-1143.

Betts, A. K., 1976: The Thermodynamic Transformation of the Tropical Subcloud Layer by Precipitation and Downdrafts. *J. Atmos. Sci.*, **33**, pp. 1008-1020.

____, 1984: Boundary layer thermodynamics of a High Plains severe storm. *Mon. Wea. Rev.*, **112**, 2199-2211.

____, 1992: FIFE Atmospheric Boundary Layer Budget Methods. *J.G.R.*, **97**, 18523-18532.

____, 1994 Relation between equilibrium evaporation and the saturation pressure budget. *Boundary-Layer Meteor*, **71**, 235-245.

____, and A.C.M. Beljaars, 1993: Estimation of roughness length for heat and momentum from FIFE data. *Atmospheric Research*, **30**, 251-261.

____, J.H. Ball, Beljaars, A.C.M., M.J. Miller and P. Viterbo, 1995: The land-surface-atmosphere interaction: a review based on observational and global modeling perspectives. *J.G.R.* (in

press).

____, J.H. Ball, and A.C.M. Beljaars, 1993: Comparison between the land surface response of the European Centre model and the FIFE-1987 data. *Q.J.R.M.S.*, **119**, 975-1001.

____, and J.H. Ball, 1994: Budget analysis of FIFE-1987 sonde data. *J.G.R.*, **99**, 3655-3666.

____, and J.H. Ball, 1995: The FIFE surface diurnal cycle climate. *J.G.R.* (in press).

Chen, F., K. Mitchell, J. Schaake, Y. Xue, H-L. Pan, V. Koren, Q. Duan, and A.Betts, 1995: Modelling of land-surface evaporation by four schemes and comparison with FIFE observations. Submitted to *J.G.R.*

Dickinson, R.E., 1984: Modeling evapotranspiration for three dimensional global climate models. in *Climate Processes and Climate Sensitivity. Geophys. Monographs 29*, Eds. J.E. Harrison and T. Takahashi, AGU, Washington DC, 58-72 .

Dorman, H.L. and P.J. Sellers, 1989: A global climatology of albedo, roughness length and stomatal resistance for atmospheric general circulation models as represented by the simple biosphere model (SiB). *J. Appl. Meteor.*, **28**, 833-855.

Grell, G.A., 1993: Prognostic evaluation of assumptions used by cumulus parameterizations. *Mon. Wea. Rev.*, **121**, 764-787.

Kalnay, E., M. Kanamitsu, R. Kistler, W. Collins, D. Deaven, L. Gandin, S. Saha, G. White, J.Woollen, Y. Zhu, M. Chelliah, W. Ebisuzaki, J. Janowiak, K.C. Mo, C. Ropelewski, J. Wang, A. Leetma, R. Reynolds, and R. Jenne, 1993: The NMC/NCAR reanalysis project. NMC. Office Note 401. available from NMC.

Kim, J., and S.B. Verma, 1990: Components of surface energy balance in a temperate grassland ecosystem, *Boundary Layer Meteorol.* **51**, 401-417.

Kalnay, E., and R. Jenne, 1991: Summary of the NMC/NCAR reanalysis workshop of April 1991. *Bull. Amer. Meteor. Soc.*, **72**, 1897-1904.

Liang, X., D. P. Lettenmaier, E. F. Wood, and S. J. Burges,1994: A simple hydrologically based model of land surface water and energy fluxes. *J. G. R.* **99**, 14415-14428.

Louis, J.F., 1979: A parametric model of vertical eddy fluxes in the atmosphere, *Bound.-Layer Meteor.*, **17**, 187-202.

Miyakoda, K. and J. Sirutis, 1986: Manual of the E-physics. Available from Geophysical Fluids Dynamics Laboratory, Princeton Univ., PO Box 308, Princeton, NJ 08542.

Mahrt, L. and H-L. Pan, 1984: A two layer model of soil hydrology. *Bound.-Layer Meteor.*, **29**, 1-20.

Monteith, J.L., 1965: Evaporation and Environment, *Symp. Soc. Exp. Biol.*, XIX, 205-234.

Pan, H-L, 1990: A simple parameterization of evapotranspiration over land for the NMC medium-range forecast model. *Mon. Wea. Rev.*, **118**, 2500-2512.

____, and L. Mahrt, 1987: Interaction between soil hydrology and boundary-Layer development. *Bound.-Layer Meteor.*, **38**, 185-202.

____, H-L., and W-S. Wu, 1994: Implementing a mass flux convection parameterization package for the NMC Medium-Range Forecast model. Tenth Conf. On Numerical Weather Prediction, July 18-22, 1994, Portland, Oregon, Amer. Meteor. Soc., 96-98.

Rutter, A.J., K.A. Kershaw, P.C. Robins, and A.J. Morton, 1971: A predictive model of rainfall interception in forests. I. Derivation of the model from a plantation of Corsican Pine. *Agric. Meteor.*, **9**, 367-384.

Sellers, P.J., Y, Mintz, Y.C. Sud, and A. Dalcher, 1986: A simple biosphere model (SiB) for use with general circulation models, *J. Atmos. Sci.*, **43**, 505-531.

_____, F.G. Hall, G. Asrar, D.E. Strebel, and R.E. Murphy, The First ISLSCP Field Experiment (FIFE), *Bull. Am. Meteorol. Soc.*, **69**(1), 22-27, 1988.

_____, and F.G. Hall, FIFE in 1992: Results, scientific gains, and future research directions, *J. Geophys. Res.*, **97**, 19,091-19,109.

Smith, E.A., W.L. Crosson, and B.D. Tanner, 1992a: Estimation of surface heat and moisture fluxes over a prairie grassland, 1, In situ energy budget measurements incorporating a cooled mirror dew point hygrometer, *J. Geophys. Res.*, **97**, 18,557-18,582.

____, A.Y. Hsu, W.L. Crosson, R.T. Field, L.J. Fritschen, R.J. Gurney, E.T. Kanemasu, W.P. Kustas, D. Nie, W.J. Shuttleworth, J.B. Stewart, S.B. Verma, H.L. Weaver, and M.L. Wesely, 1992b: Area-Averaged surface fluxes and their time-space variability over the FIFE experimental domain, *J. Geophys. Res.*, **97**, 18599-18622.

Strebel, D. E., D.R. Landis, K.F. Huemmrich, and B.W. Meeson, 1994: Collected data of the First ISLSCP Field Experiment, in *Surface Observations and Non-Image Data Sets*,. vol. 1, CD-ROM, NASA Goddard Space Flight Center, Greenbelt, MD 20771.

Sugita, M., and W. Brutsaert, 1990a: Wind velocity measurements in the neutral boundary layer above hilly prairie. *J. Geophys. Res.*, **95**, 7617-7624.

_____, and W. Brutsaert, 1990b: How similar are temperature and humidity profiles in the unstable boundary layer? *J. Appl. Meteorol.*, **29**, 489-497.

Viterbo, P. and Beljaars, A.C.M. A new land surface parameterization scheme in the ECMWF model and its validation, (submitted to *J. Clim.*, 1995).

List of Figures:

Fig 1 Comparison of daily averages of incoming solar radiation (S↓ upper curves) from FIFE (solid) and MRF reanalysis (dashed) for 1987. Lower curves are daily precipitation (in mm) with data solid and model dashed.

Fig 2 As Fig 1 for net radiation (RNet) and ground heat flux as (-G).

Fig 3 As Fig 1 for sum of surface sensible (SH) and latent heat (LH) flux.

Fig 4 As Fig 1 for SH and LH fluxes.

Fig 5 Comparison of nighttime averages (00-12 UTC) of SH and LH fluxes (middle curves). Lower curves show daily precipitation; upper curve is model wind at 06 UTC.

Fig 6 Daytime averages (12-24 UTC) of LH and SH (sign reversed) fluxes. Middle curves are daily total precipitation.

Fig 7 Surface Bowen ratio (BR) comparison. Upper curve shows daily total precipitation.

Fig 8 Comparison of monthly averaged daytime diurnal cycle of surface potential temperature and moisture at 2 m.

Fig 9 Comparison of monthly averaged surface θ_E (equivalent potential temperature) and P_{LCL} (pressure height of LCL above surface).

Fig 10 Comparison of diurnal cycle of surface wind speed for June, July, August average; and September, October average.

Fig 11 Daytime diurnal cycle (on θ, q plot) for MRF for 6-day average June 18-23 compared with group of 3 dry days (June 19, 21 and 23) and 3 days with afternoon showers (June 18, 20 and 22).

Fig 12 48-hr forecast from 12 UTC on June 20, showing components of the model surface energy and LH budgets, together with model precipitation.

Fig 13 Model forecast profiles of θ_E, θ_{ES} for the morning of June 211 at 1445, 1645 and 1845 UTC (Local noon is 1820 UTC).

Fig 14 Comparison of average model 24-hr forecasts from 12 UTC on June 26 and 27 with FIFE data for same periods.

Fig 15a As Fig 14 for profiles of θ against pressure, showing selected times in the daytime diurnal cycle.

Fig 15b As Fig 15a for profiles of q against pressure.

Fig 16 Daytime diurnal cycle of θ and q for FIFE data (solid) and MRF (dashed) for June 26-27 average.

Fig 17 As Fig 16 for averages of July 30 and 31: data is hourly starting at 1215 UTC.

Fig 18 Comparison of $\Delta T=T_{Surf}-T$ for model and data for July 30-31 average.

Fig 19 As Fig 14 for July 30 and 31.

Fig 20 Comparison of net radiation and ground heat flux for 9-day August average for 24-hr MRF forecasts and FIFE data.

Fig 21 As Fig 20 for SH and LH fluxes.

Fig 22 As Fig 20 for a (θ,q) plot of the daytime diurnal cycle.

Fig 23 Soil moisture at local noon for selected days for the two model layers in reanalysis (in % by volume).

Fig 24 Comparison of daytime surface BR for model and FIFE data for forecasts from 12 UTC on August 9 and 10 (average) and August 15.

Fig 25 As Fig 24 for SH 24-hr forecasts of flux.

Fig 26 As Fig 25 for LH flux.

Fig 27 Model surface transfer coefficients for momentum (C_d) and heat and moisture (C_h) for August 9-10 average and August 15.

Fig 28 As Fig 25 for surface wind comparison.

Fig 29 As Fig 28 for $\Delta T=T_{surf}-T$.

Fig 30 As Fig 16 for August 9-10 average and August 15.

Fig 31a As Fig 15a for θ profile for August 9-10 average.

Fig 31b As Fig 31a for q profile.

Fig 32a As Fig 31a for August 15.

Fig 32b As Fig 31b for August 15.

Fig 33 BL wind speed profiles for August 15 for model and FIFE data.

Fig 34 As Fig 16 for October 7-8 average.

Fig 35 As Fig 14 for October 7-8 average.

Fig 36 Comparison of SH flux for three averages of model forecasts and FIFE data for 3 pairs of days through season.

Fig 37 As Fig 36 for 2-m air temperature comparison.

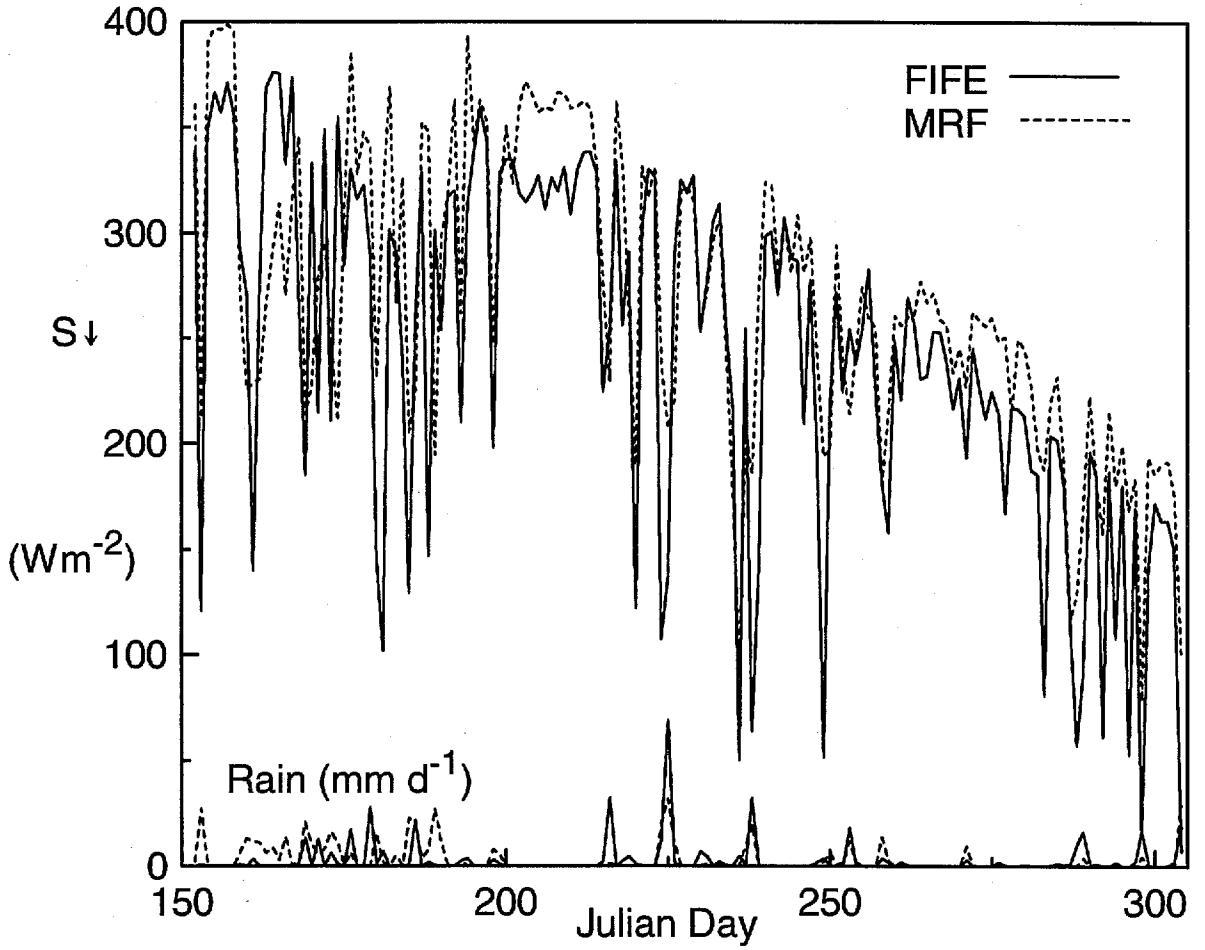

Jul 13 1995

FIG1_HDF

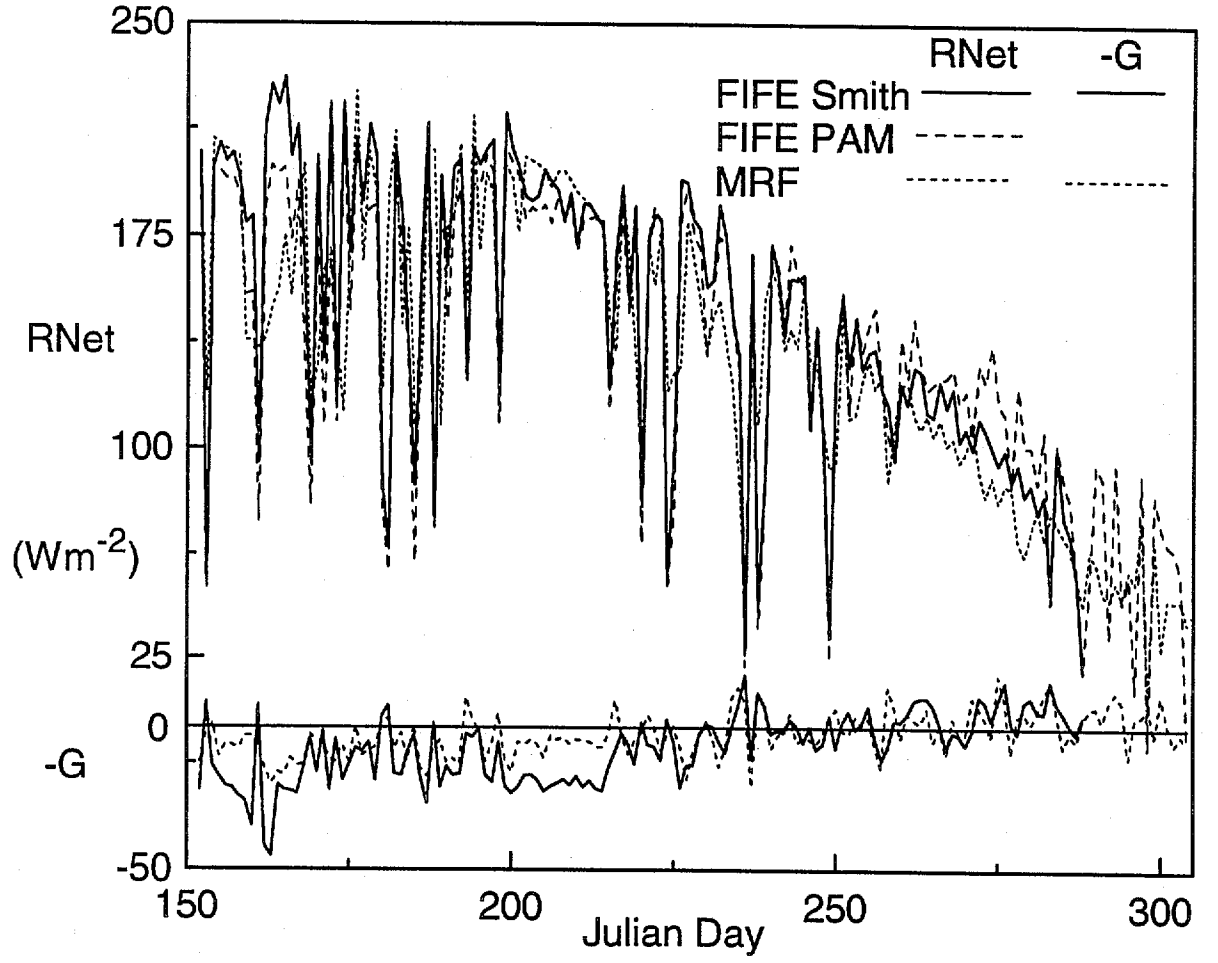

Jul 11 1995

FIG2_HDF

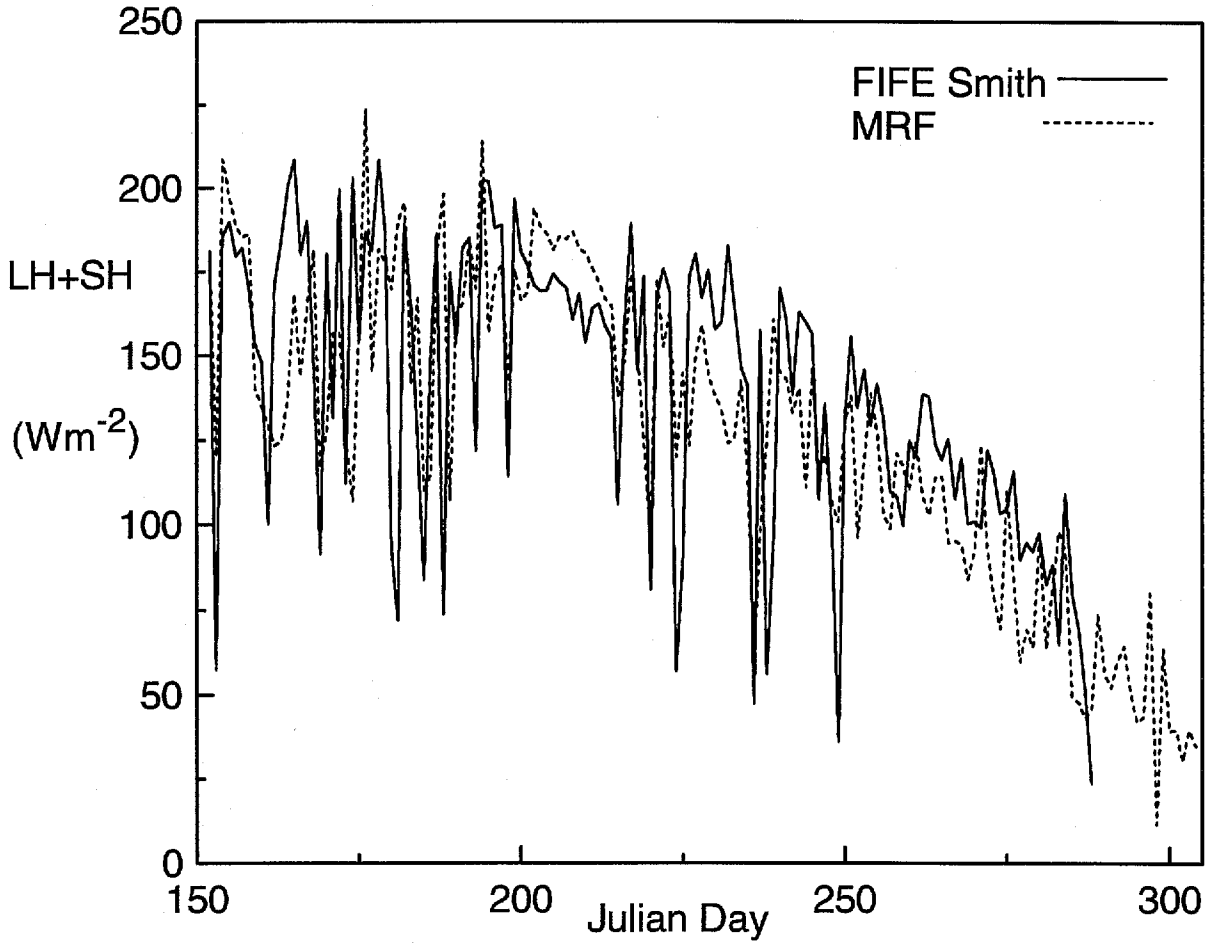

Jul 13 1995

FIG3_HDF

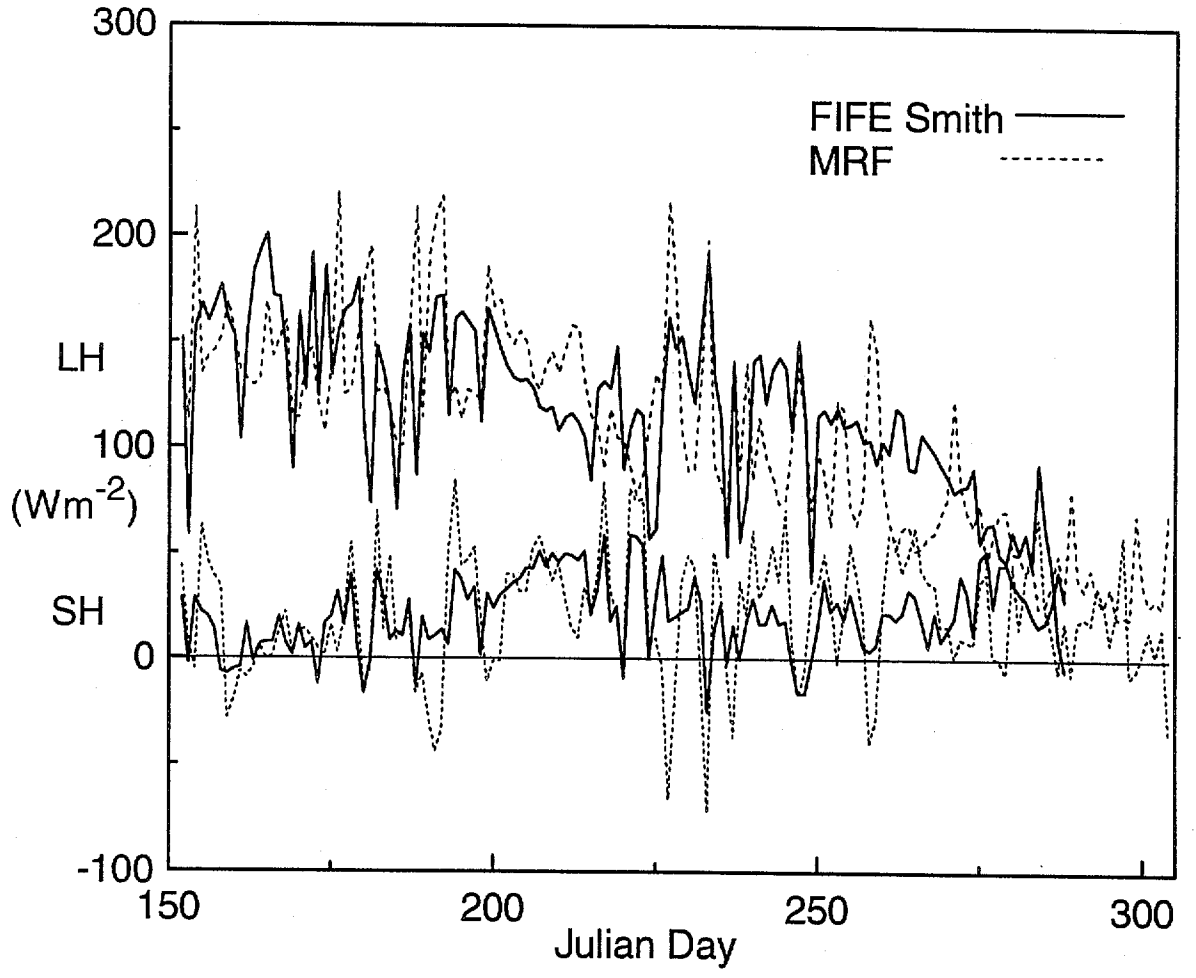

Jul 11 1995

FIG4_HDF

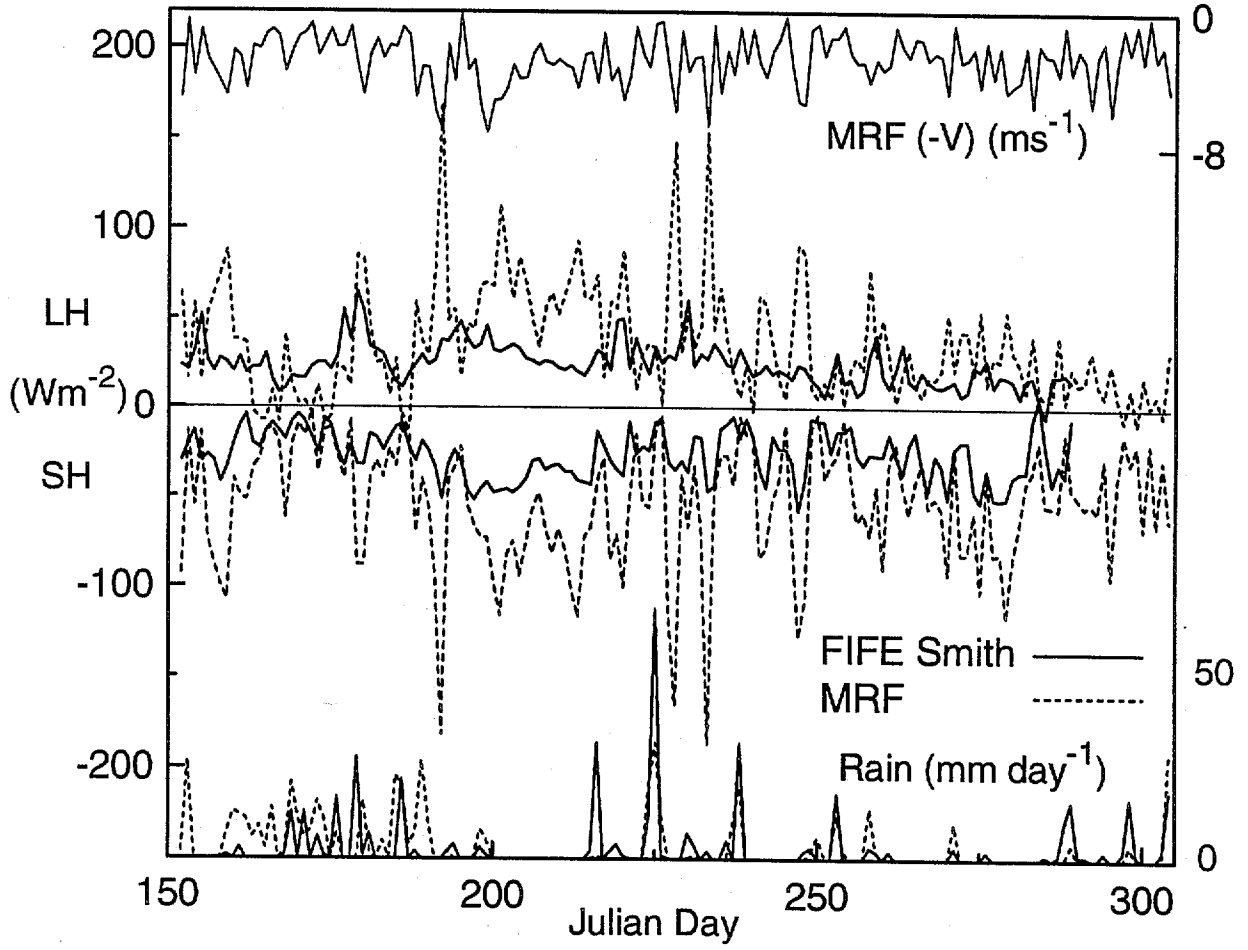

Jul 11 1995

FIG5_HDF

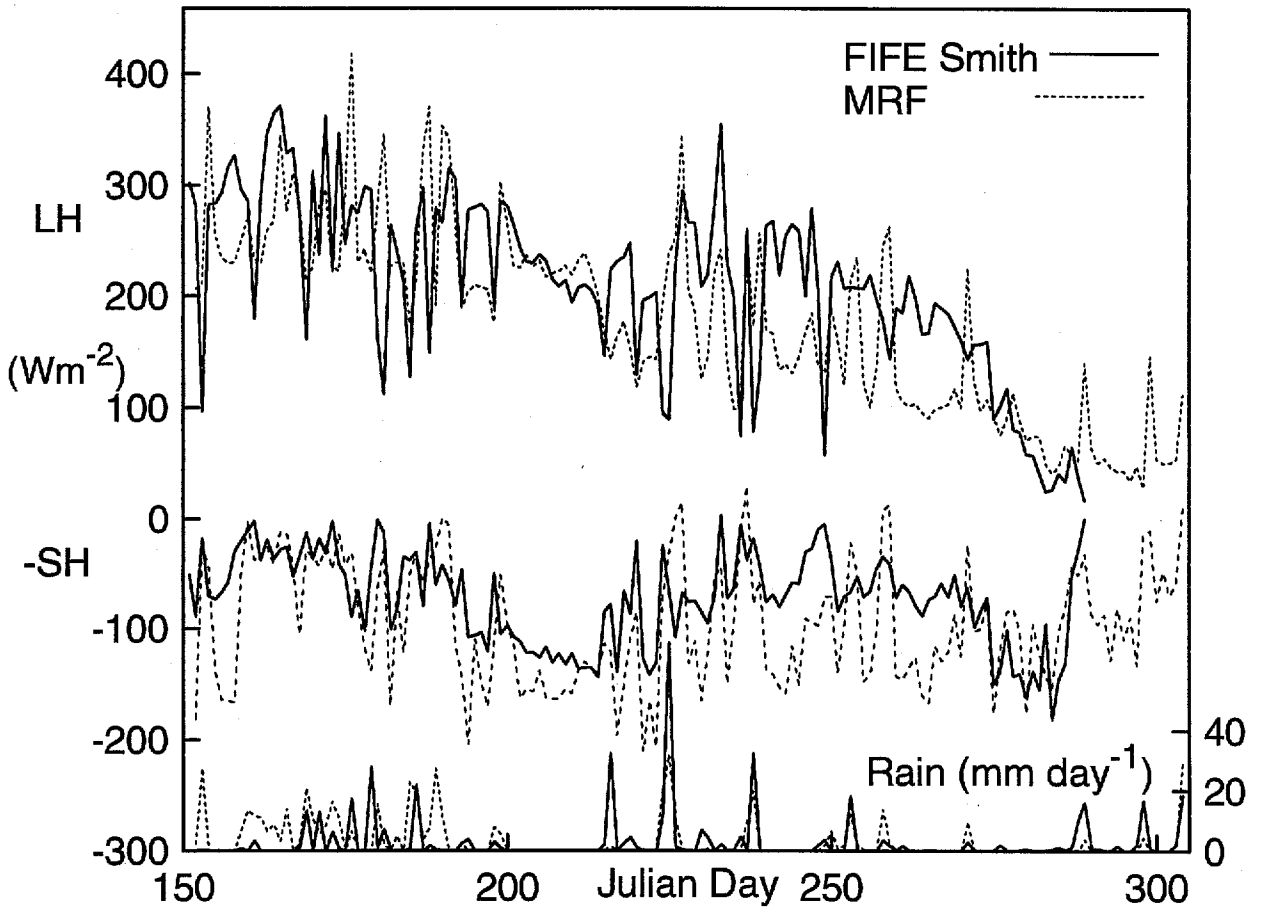

Jul 13 1995

FIG6_HDF

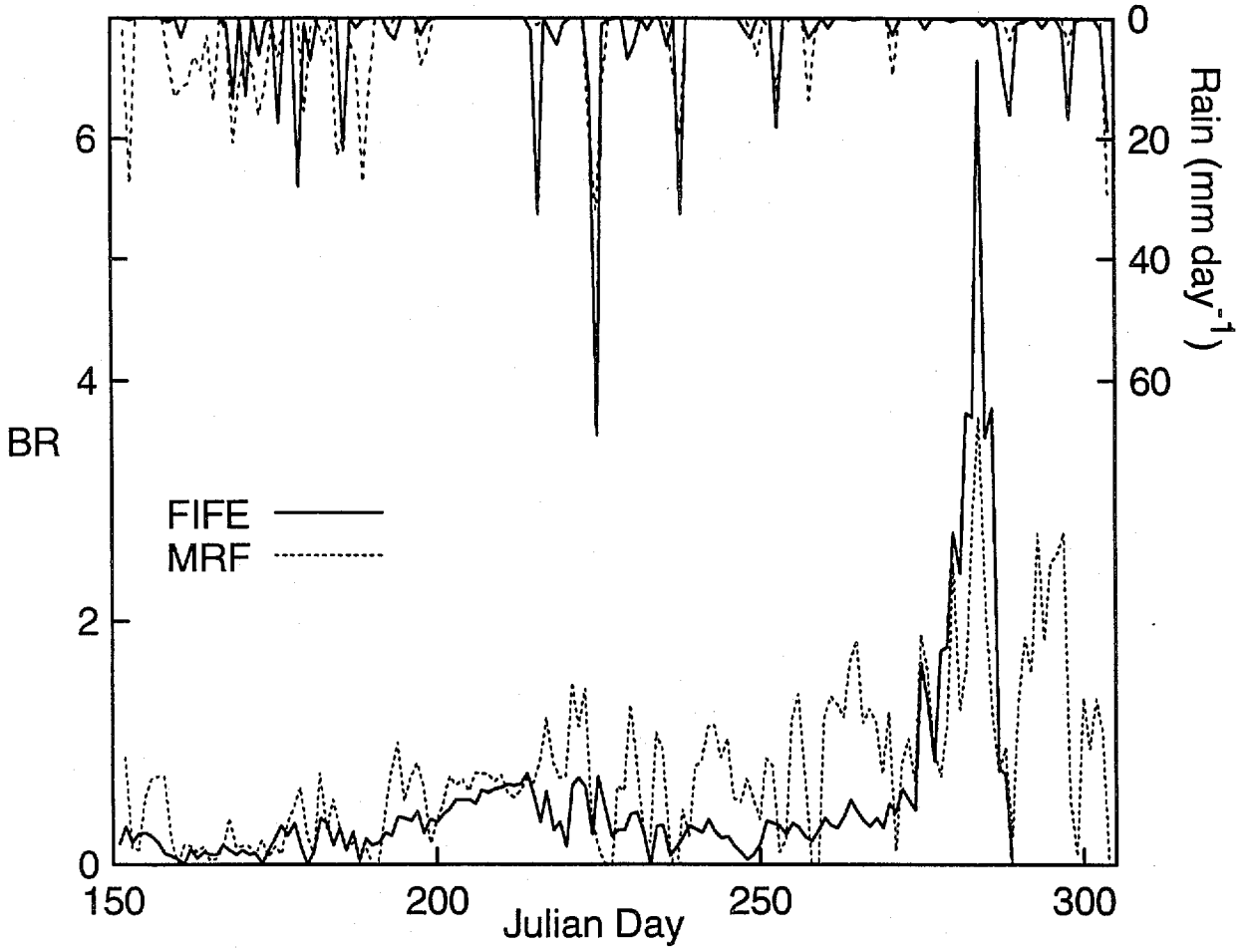

Jul 12 1995

FIG7_HDF

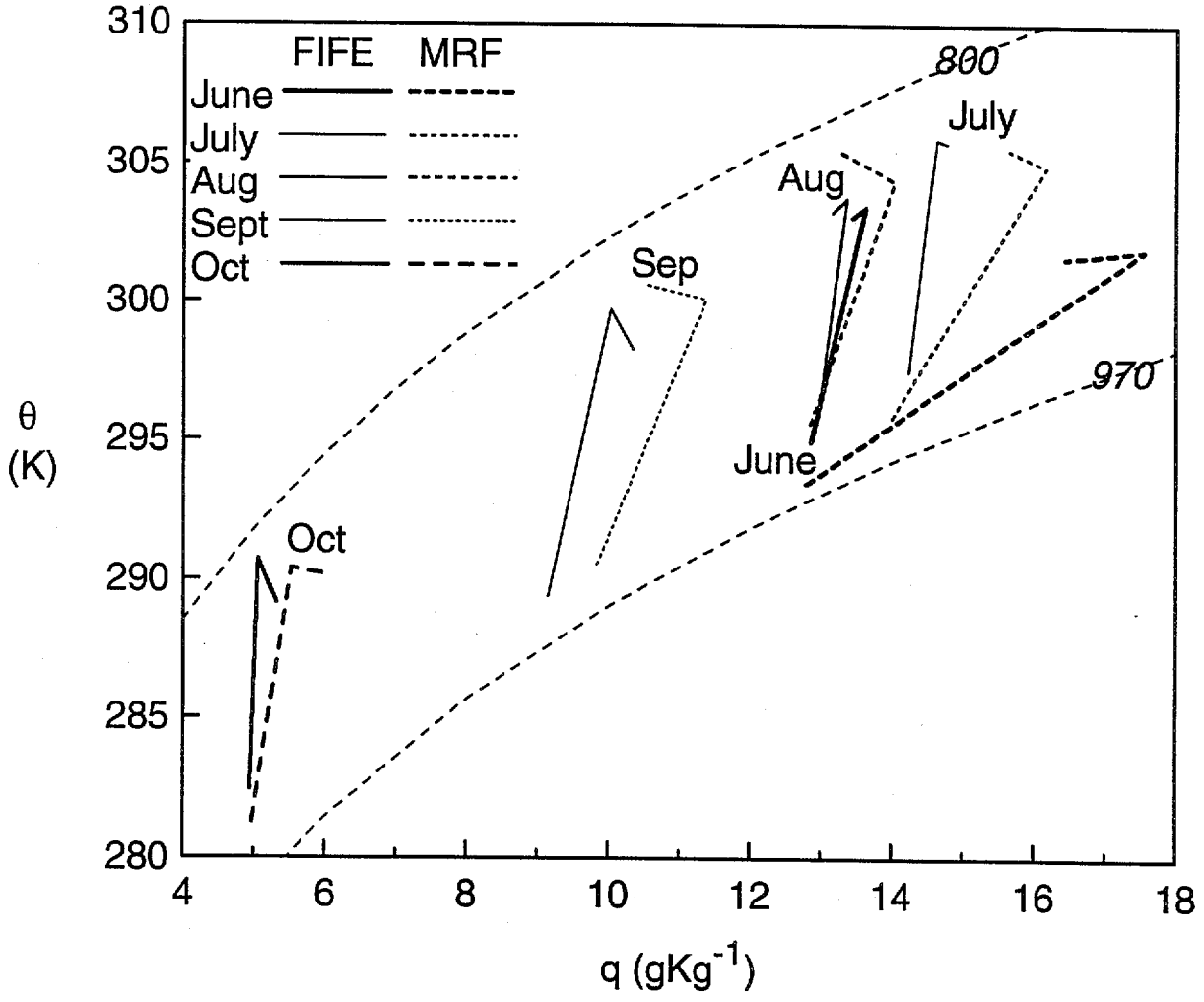

Jul 12 1995

FIG8_HDF

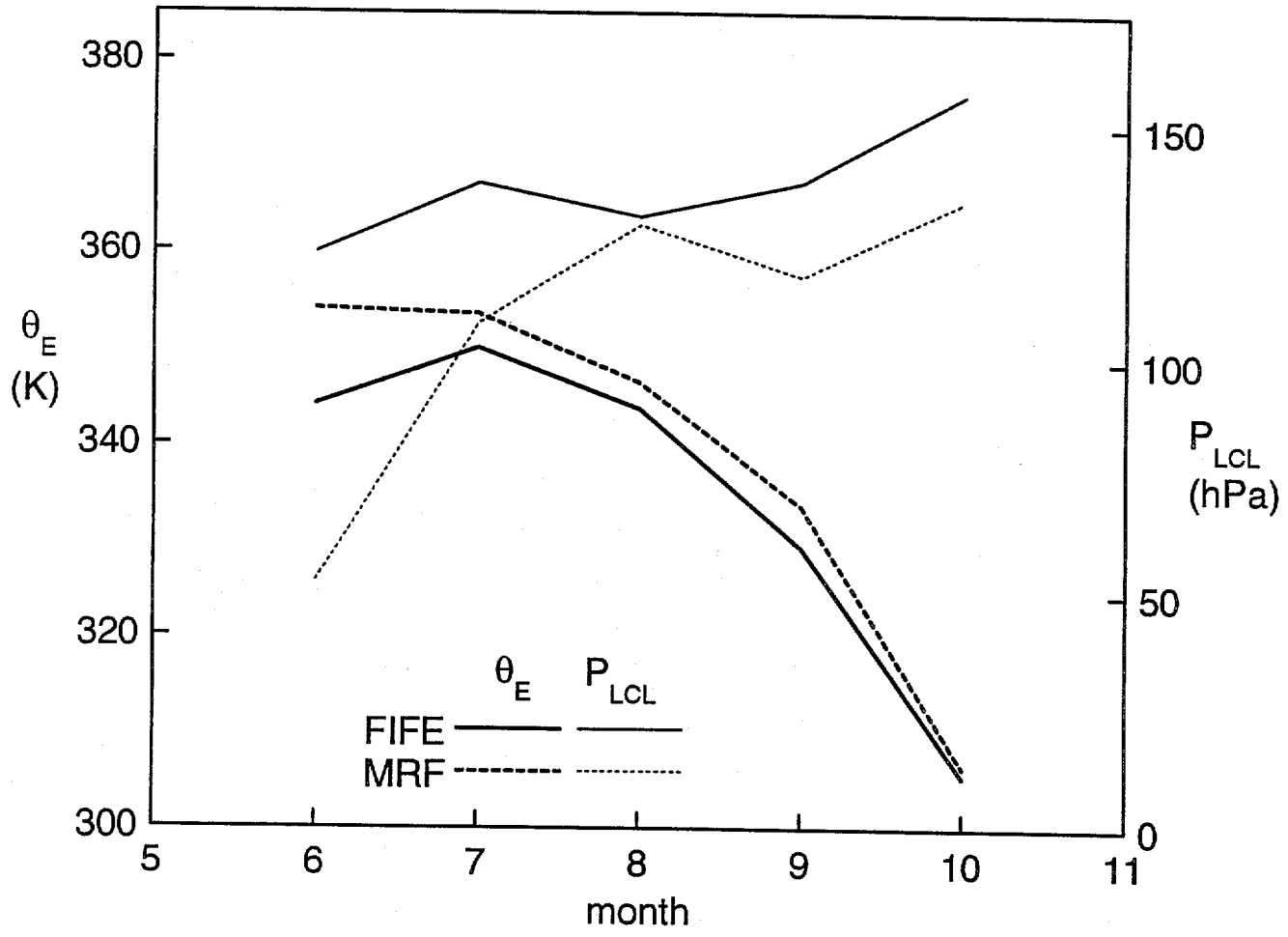

Jul 12 1995

FIG9_HDF

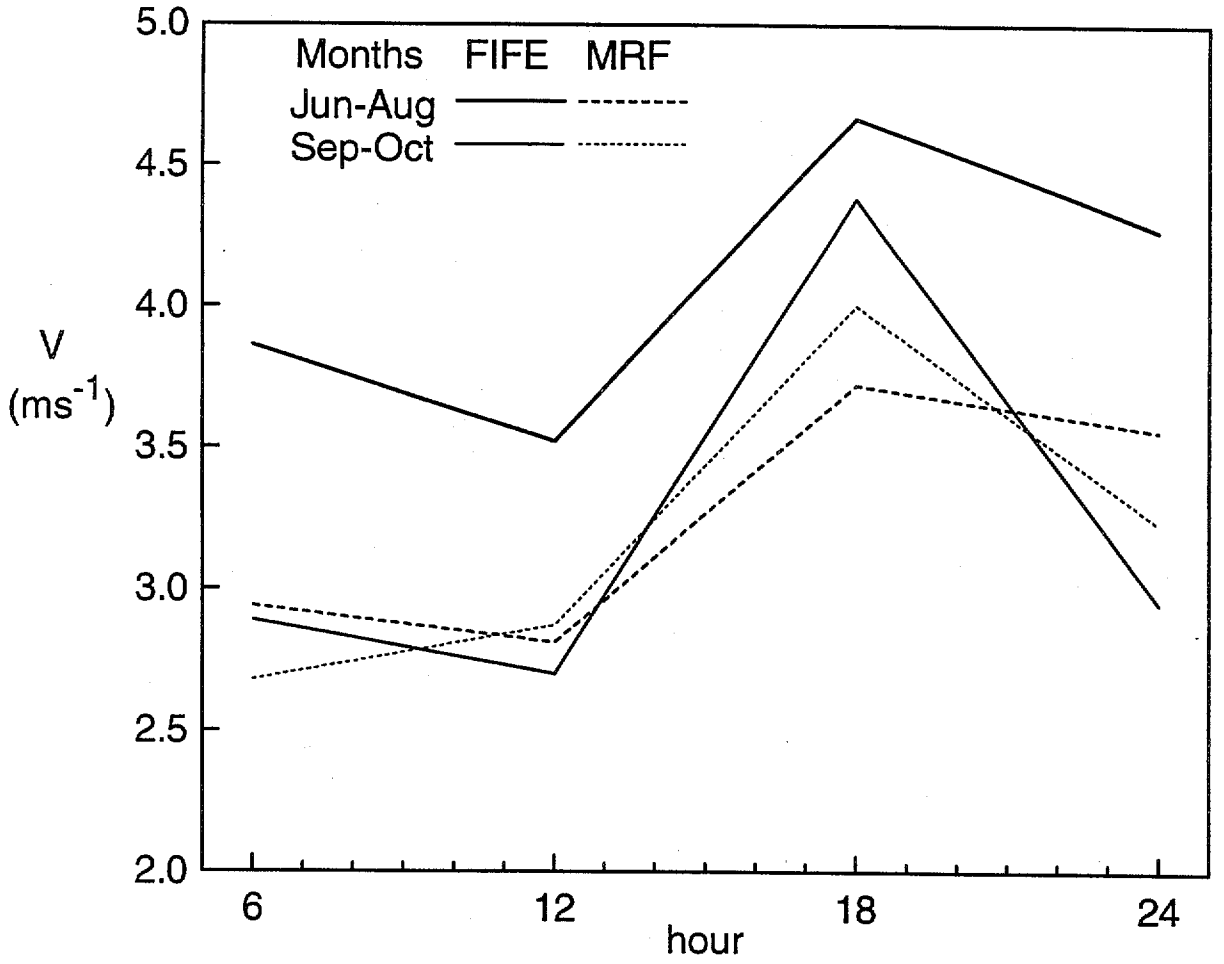

Jul 12 1995

FIG10_HDF

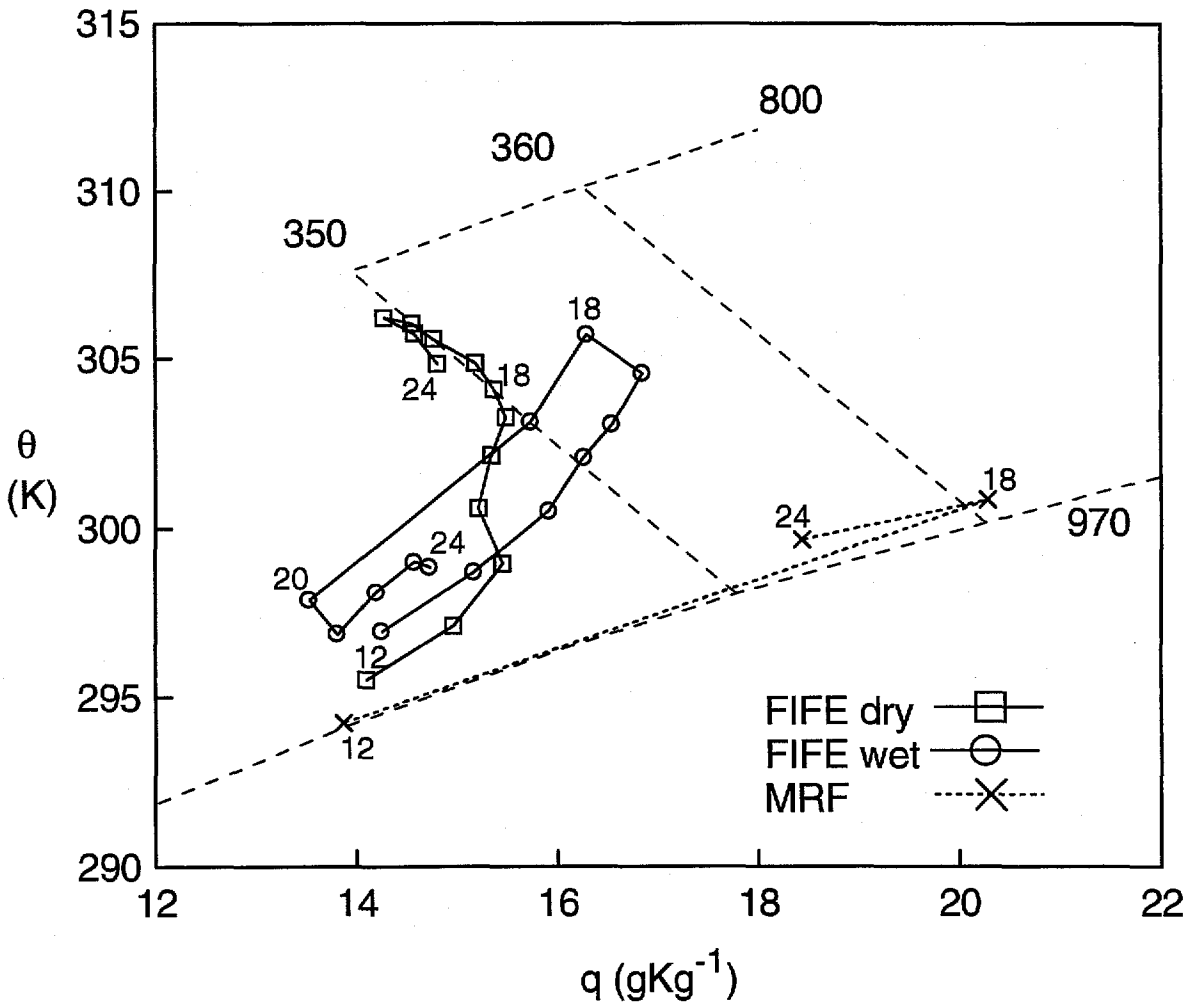

Jul 13 1995

FIG11_HDF

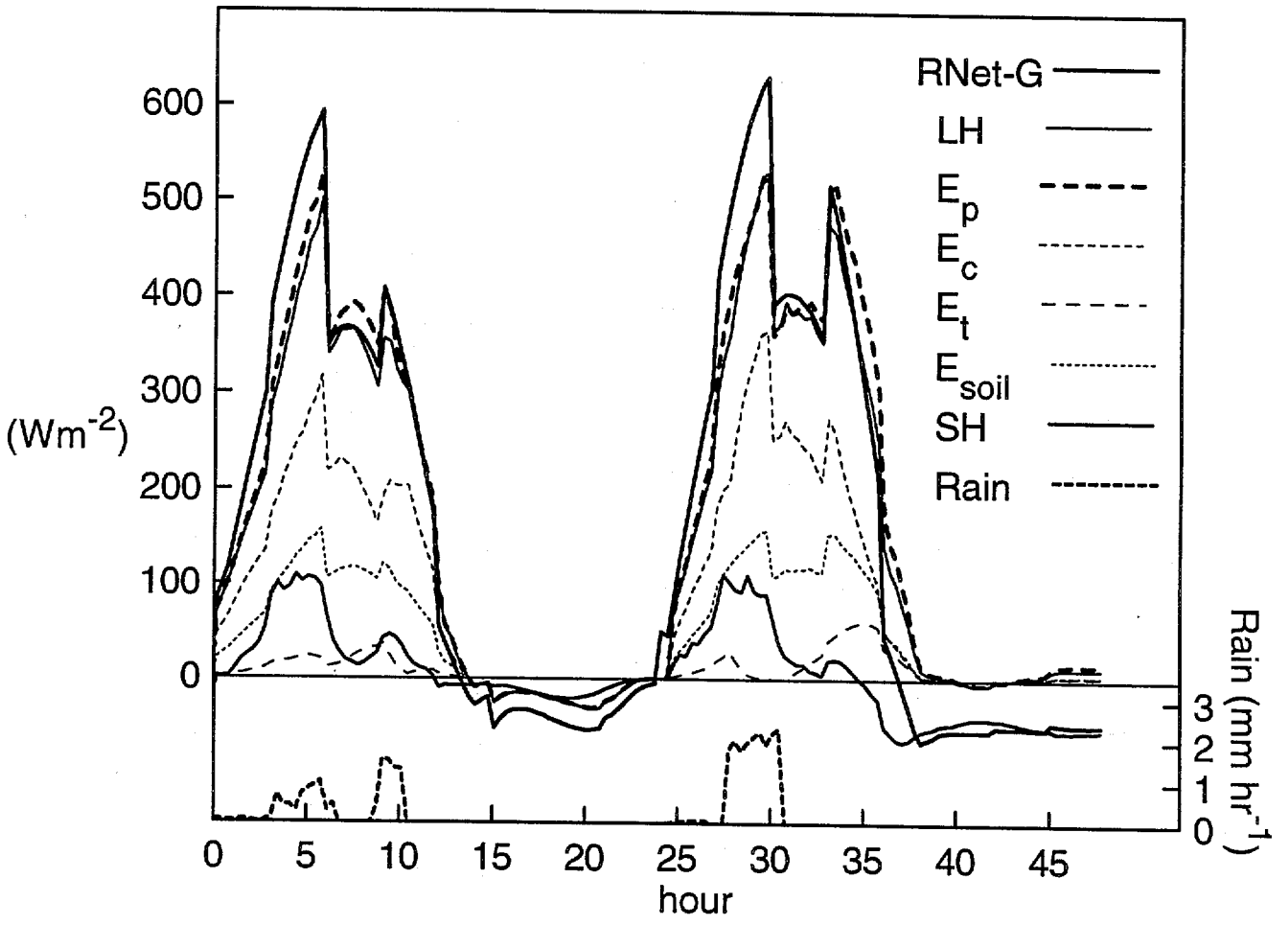

Jul 12 1995

FIG12_HDF

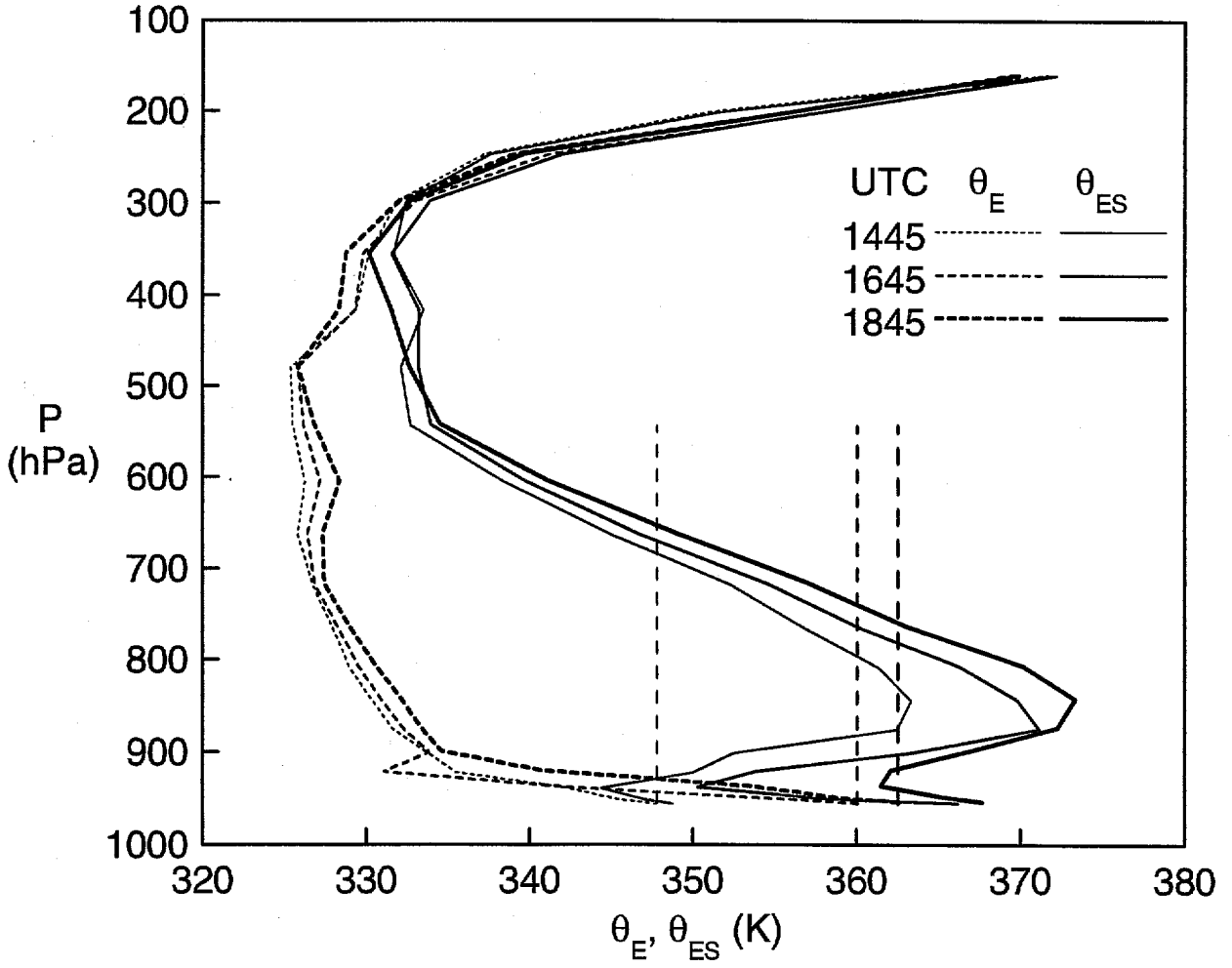

Jul 13 1995

FIG13_HDF

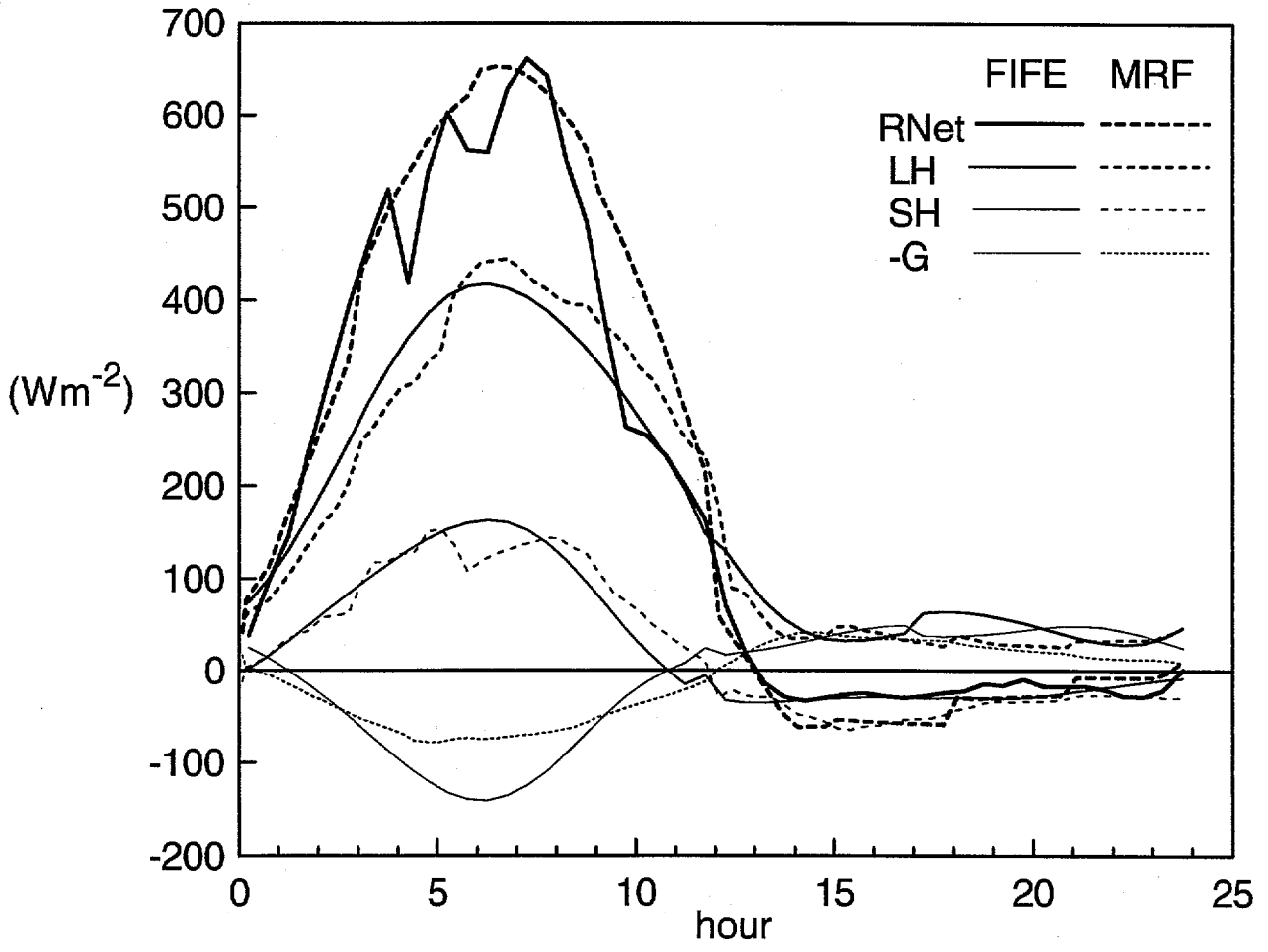

Jul 13 1995

FIG14_HDF

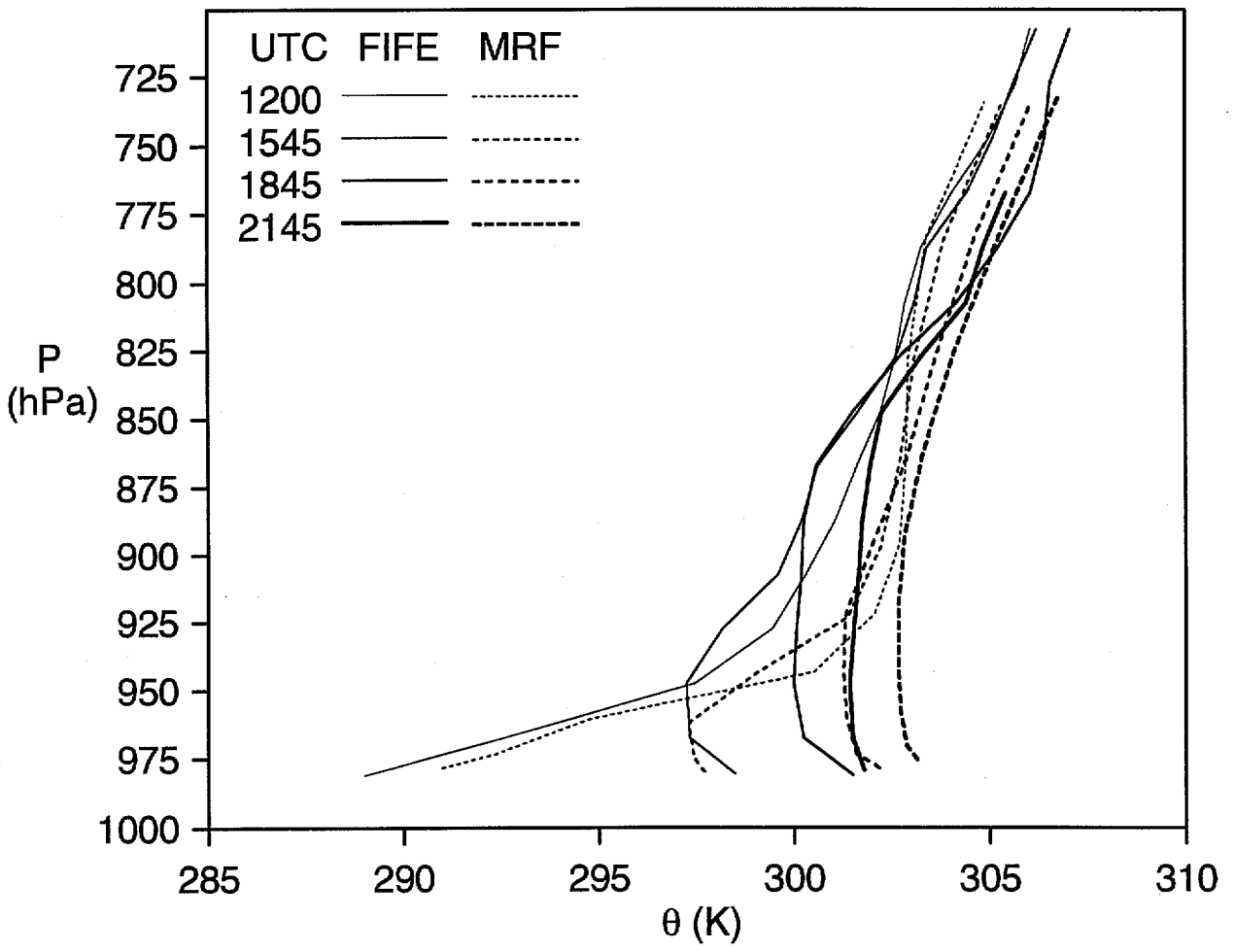

Jul 13 1995

FIG15A_HDF

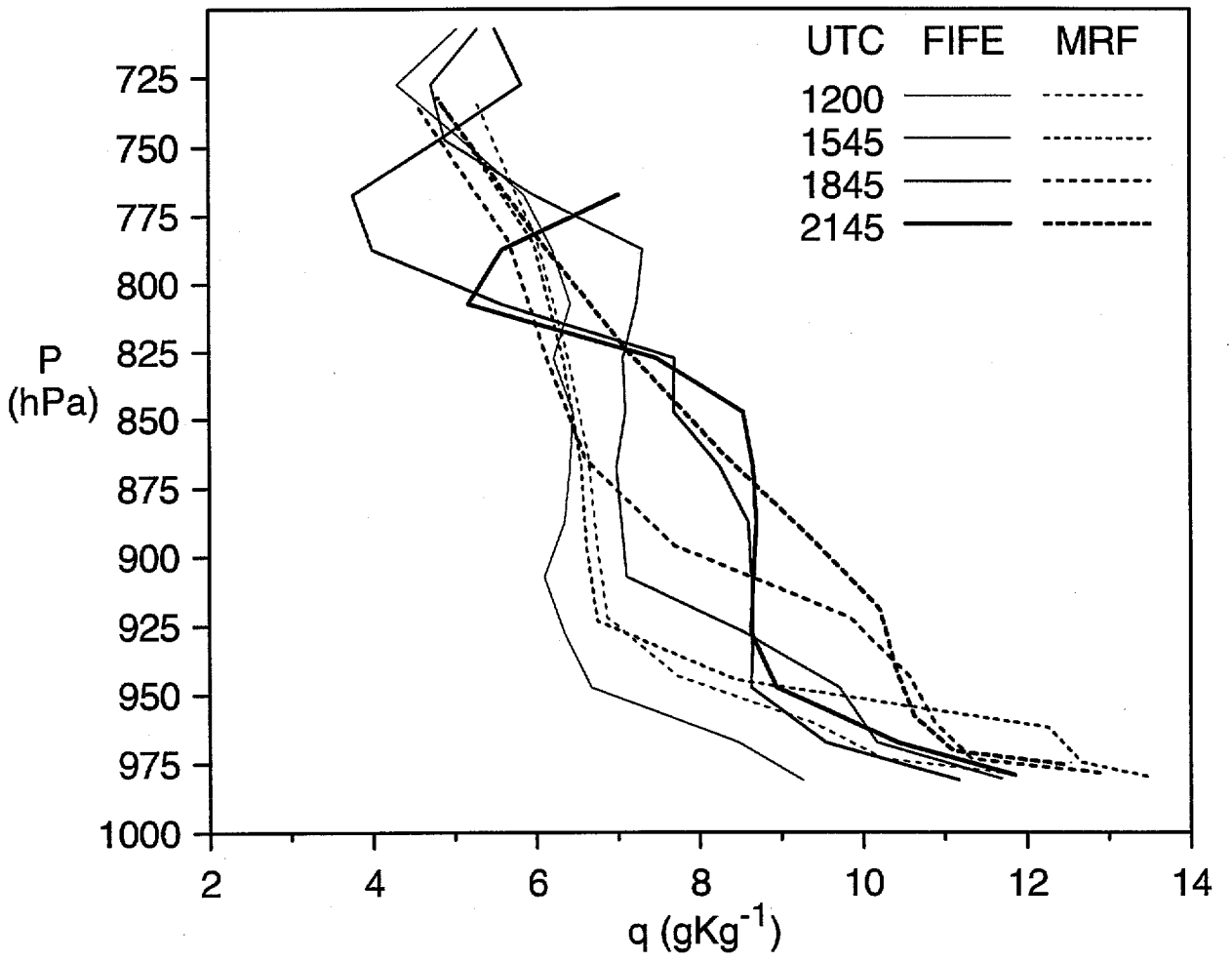

Jul 13 1995

FIG15B_HDF

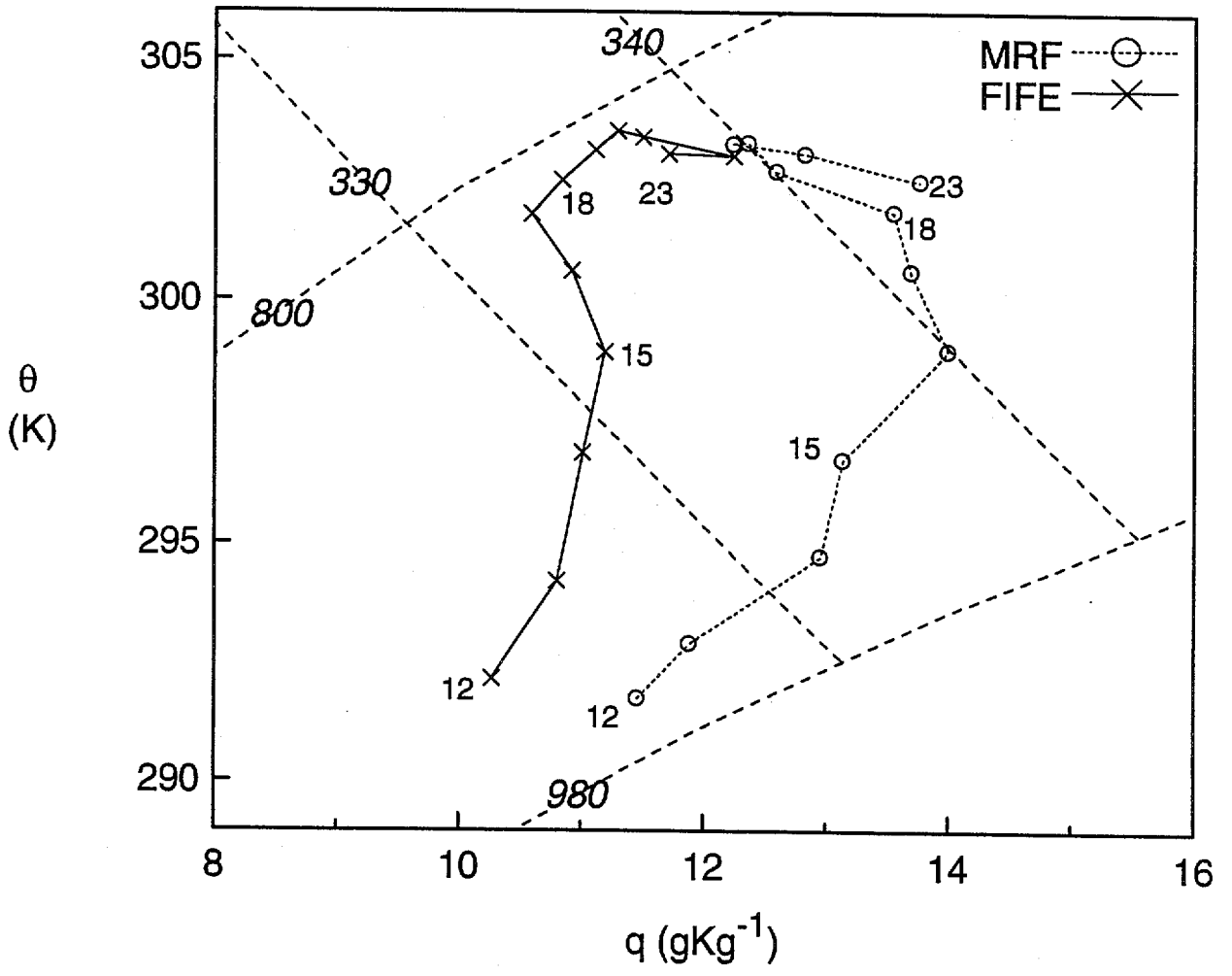

Jul. 12 1995

FIG16_HDF

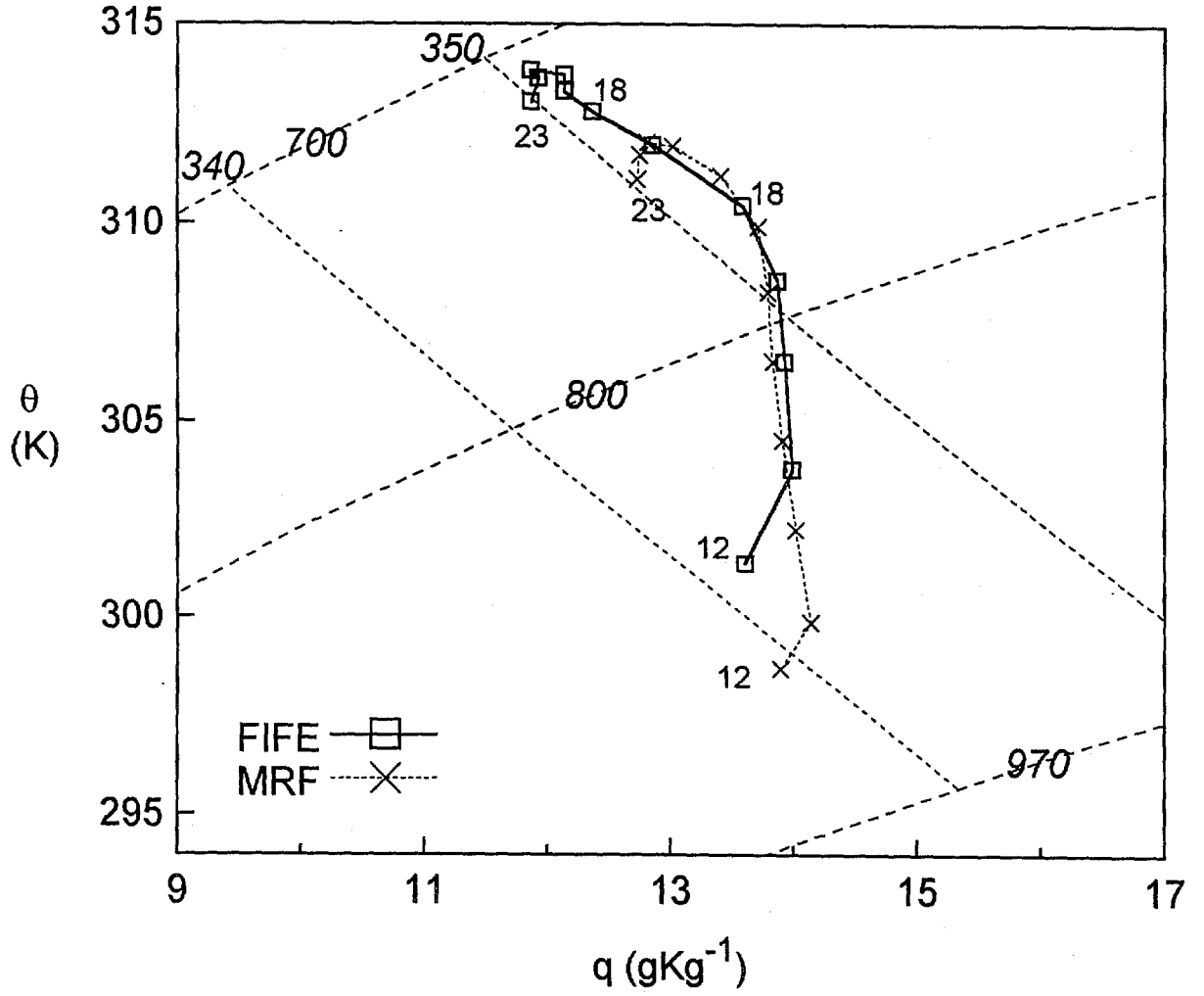

Jul. 12 1995

FIG17_HDF

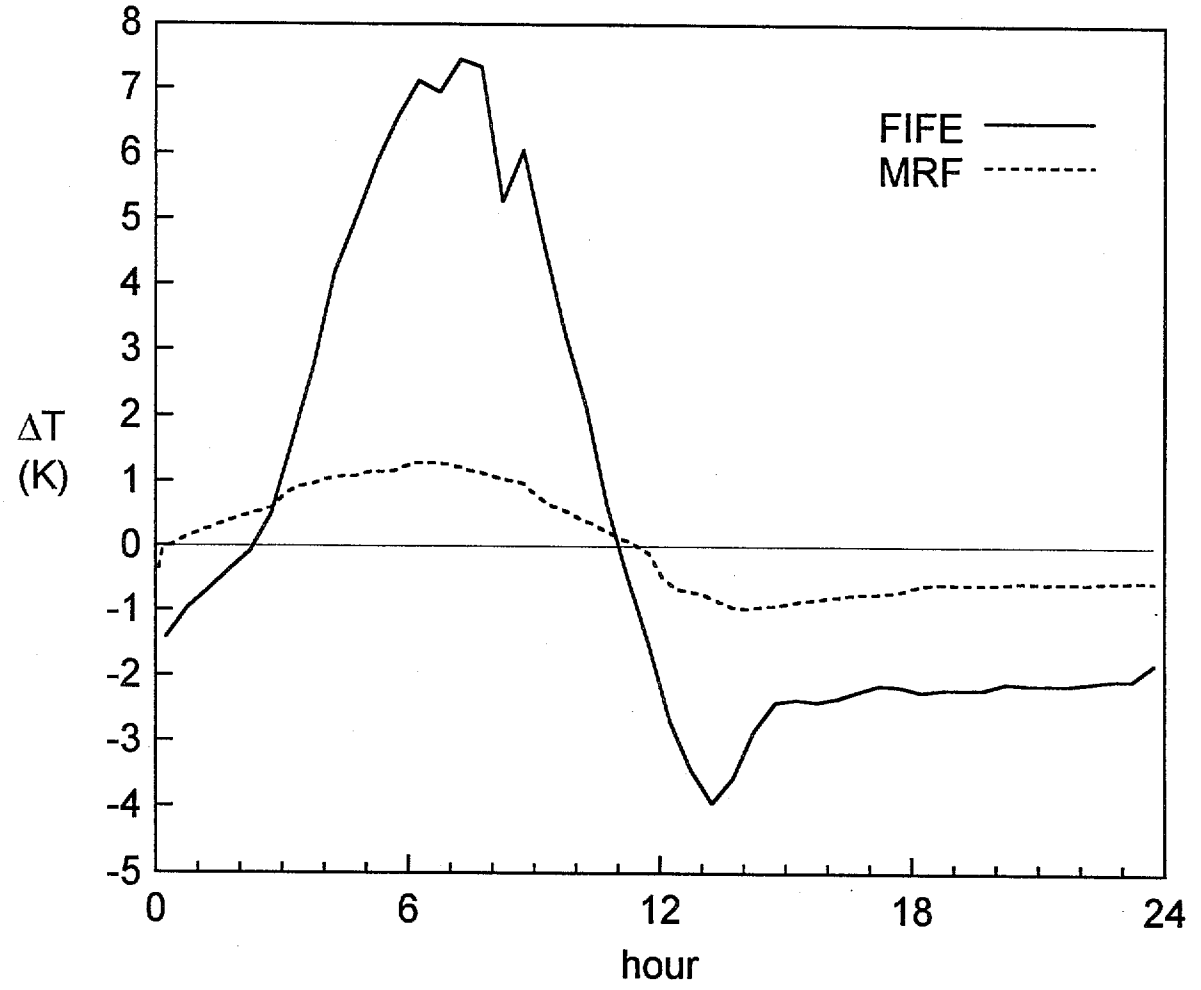

Jul. 12 1995

FIG18_HDF

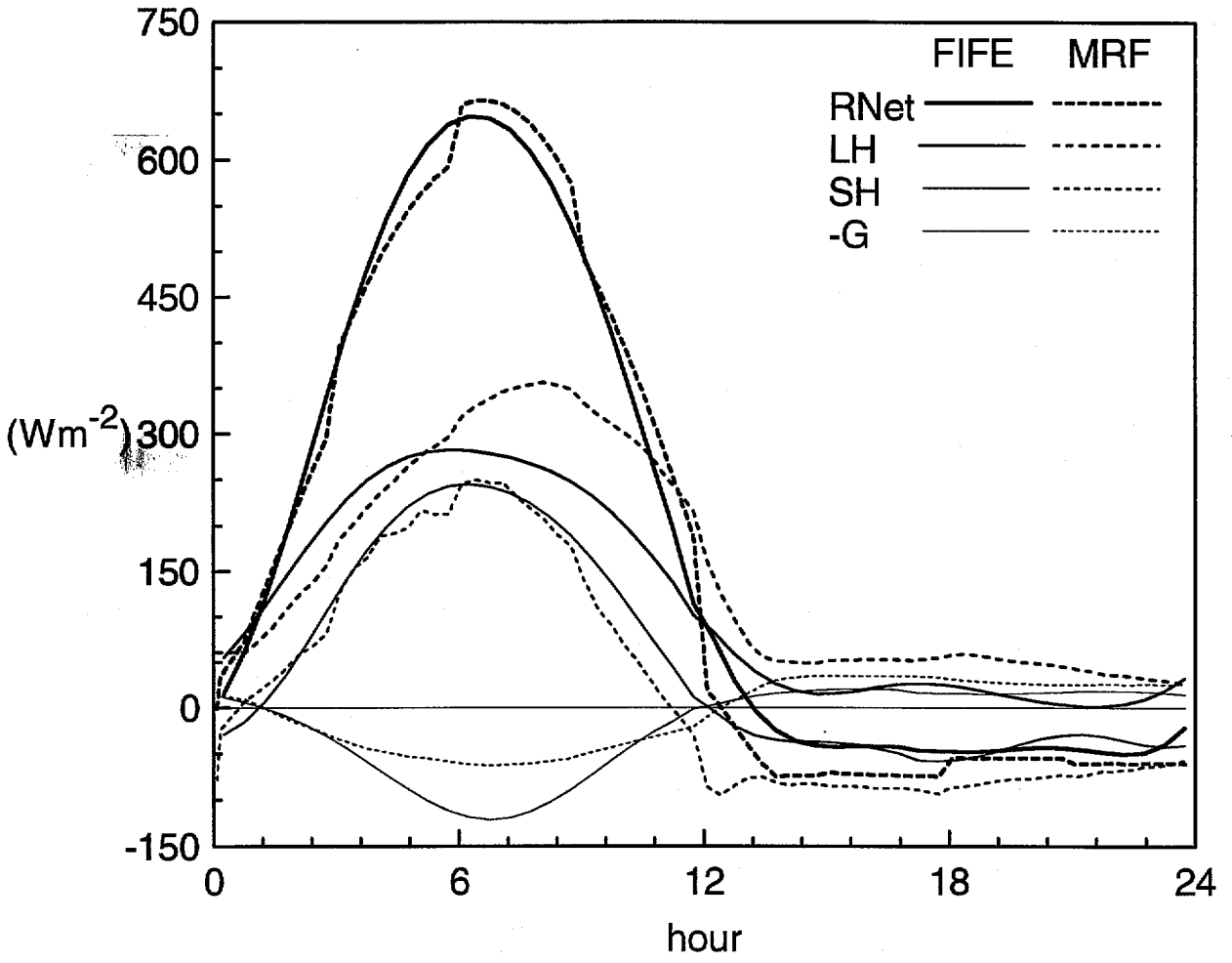

Jul 13 1995

FIG19_HDF

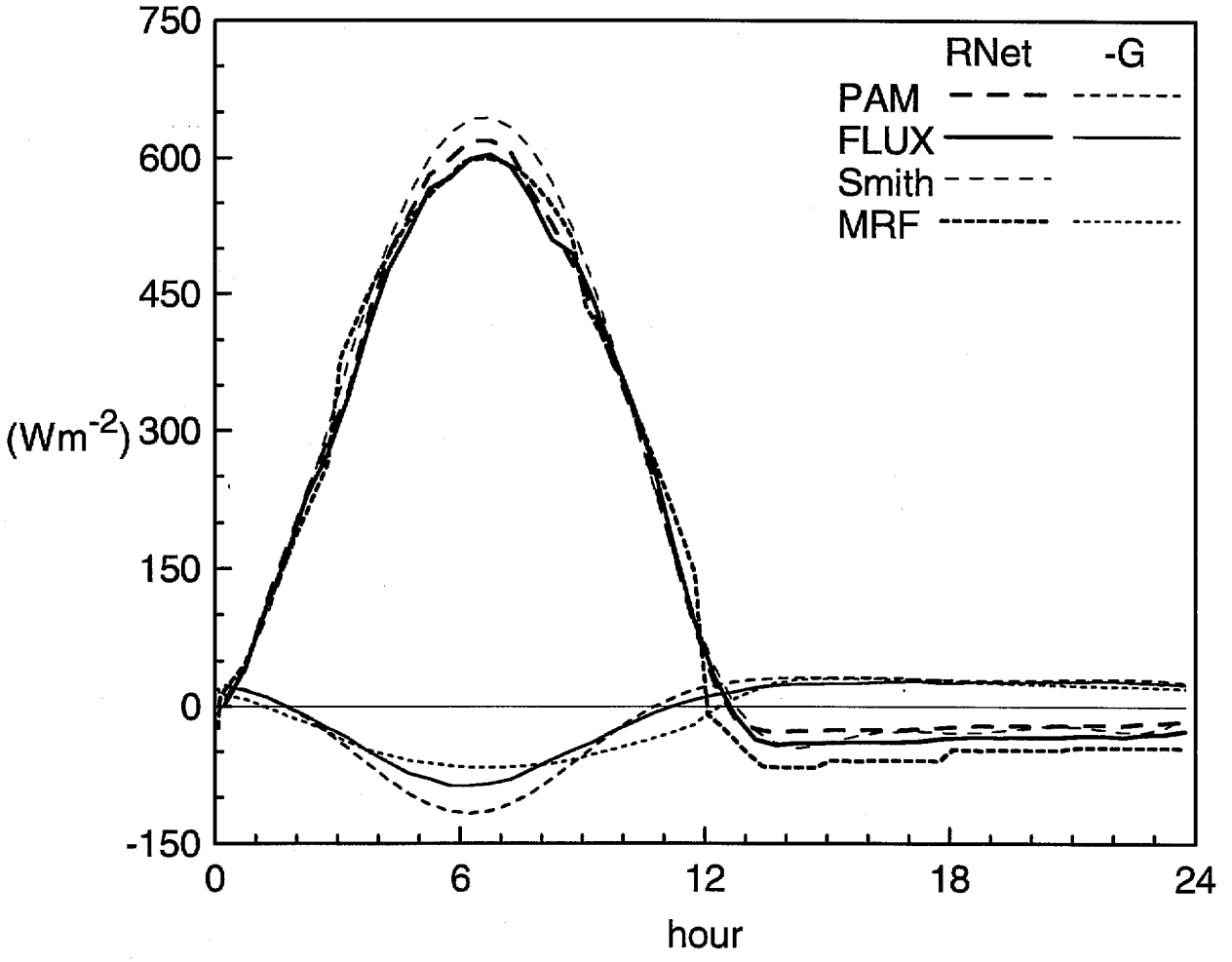

Jul 13 1995

FIG20_HDF

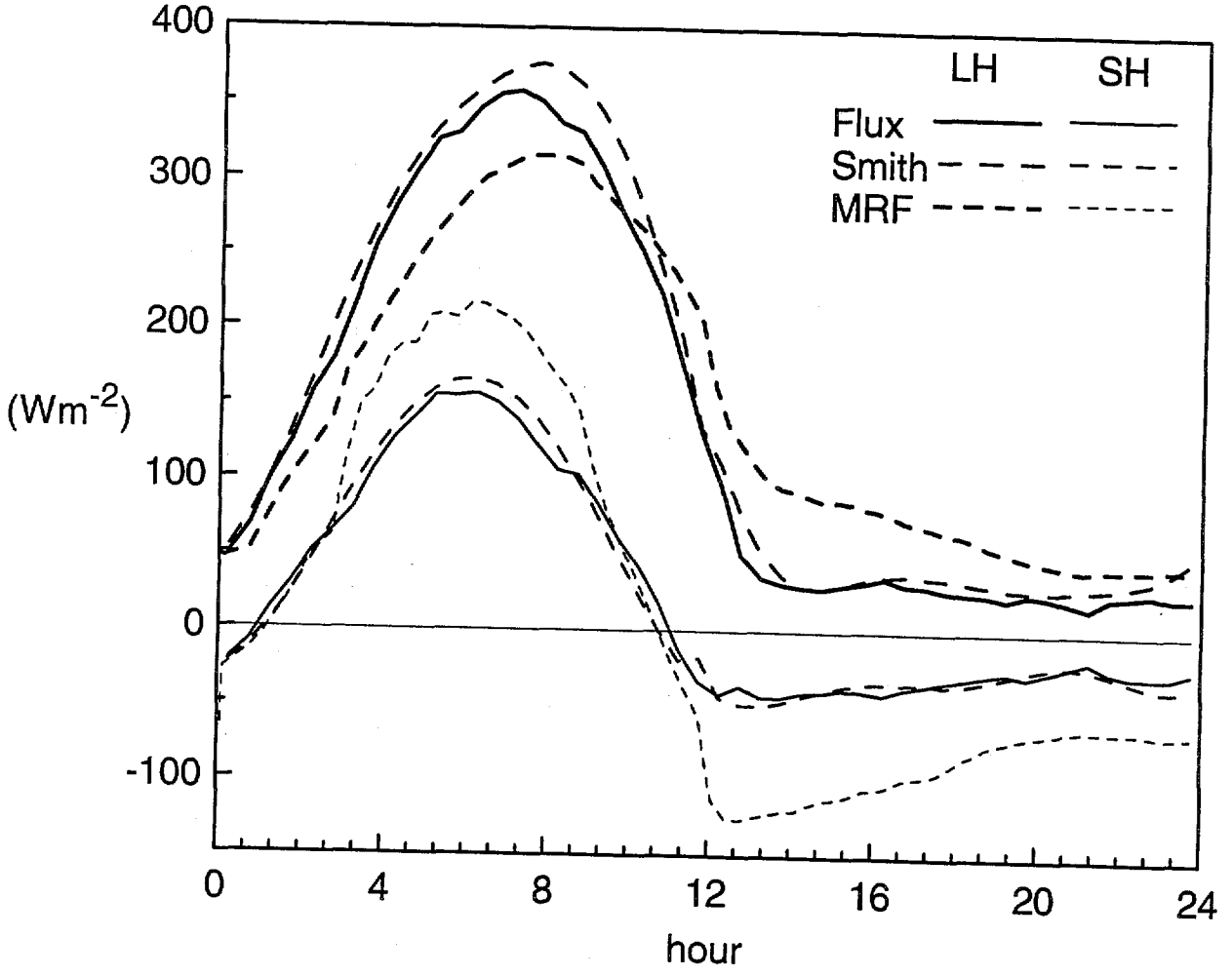

Jul. 12 1995

FIG21_HDF

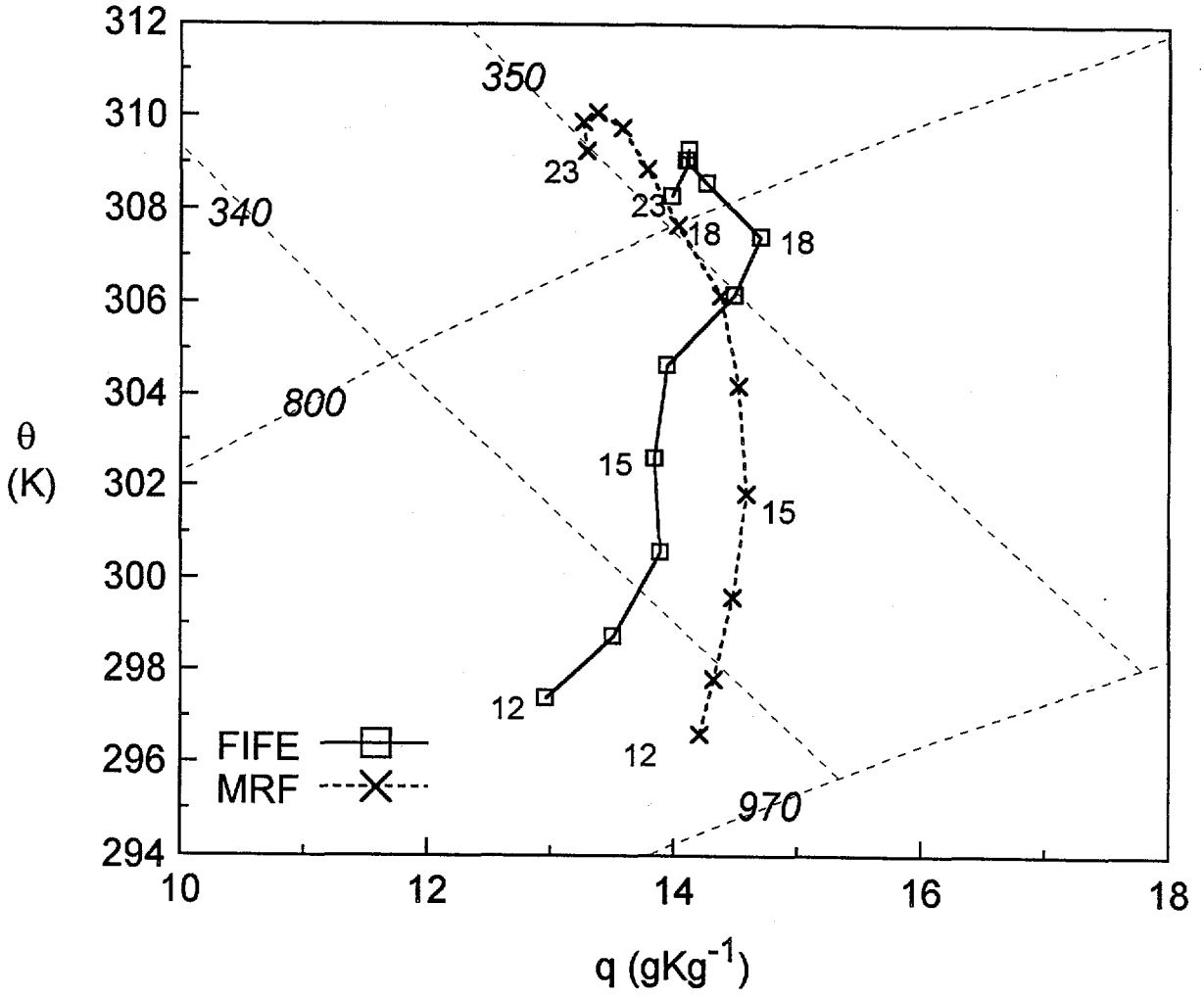

Jul. 12 1995

FIG22_HDF

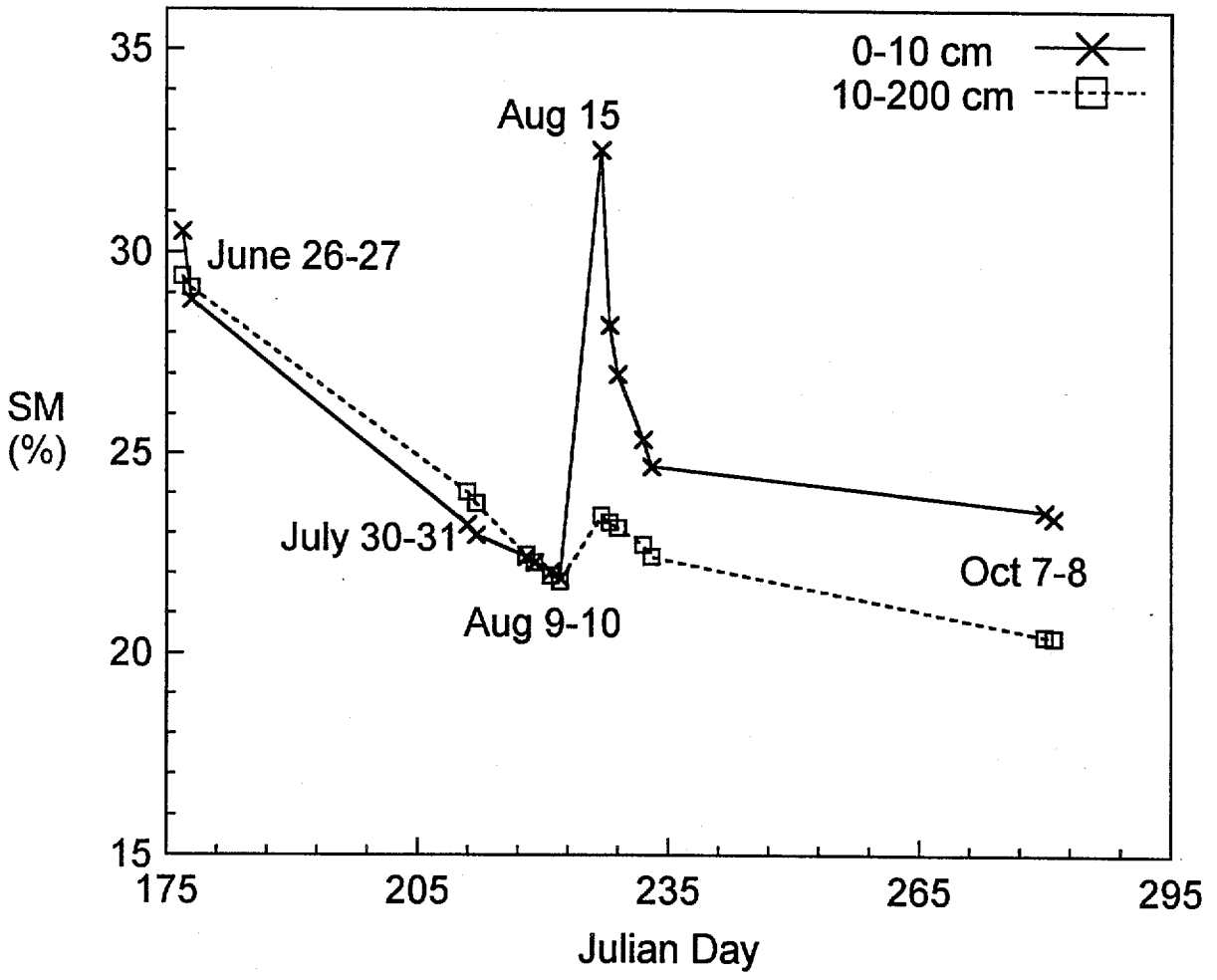

Jul. 12 1995

FIG23_HDF

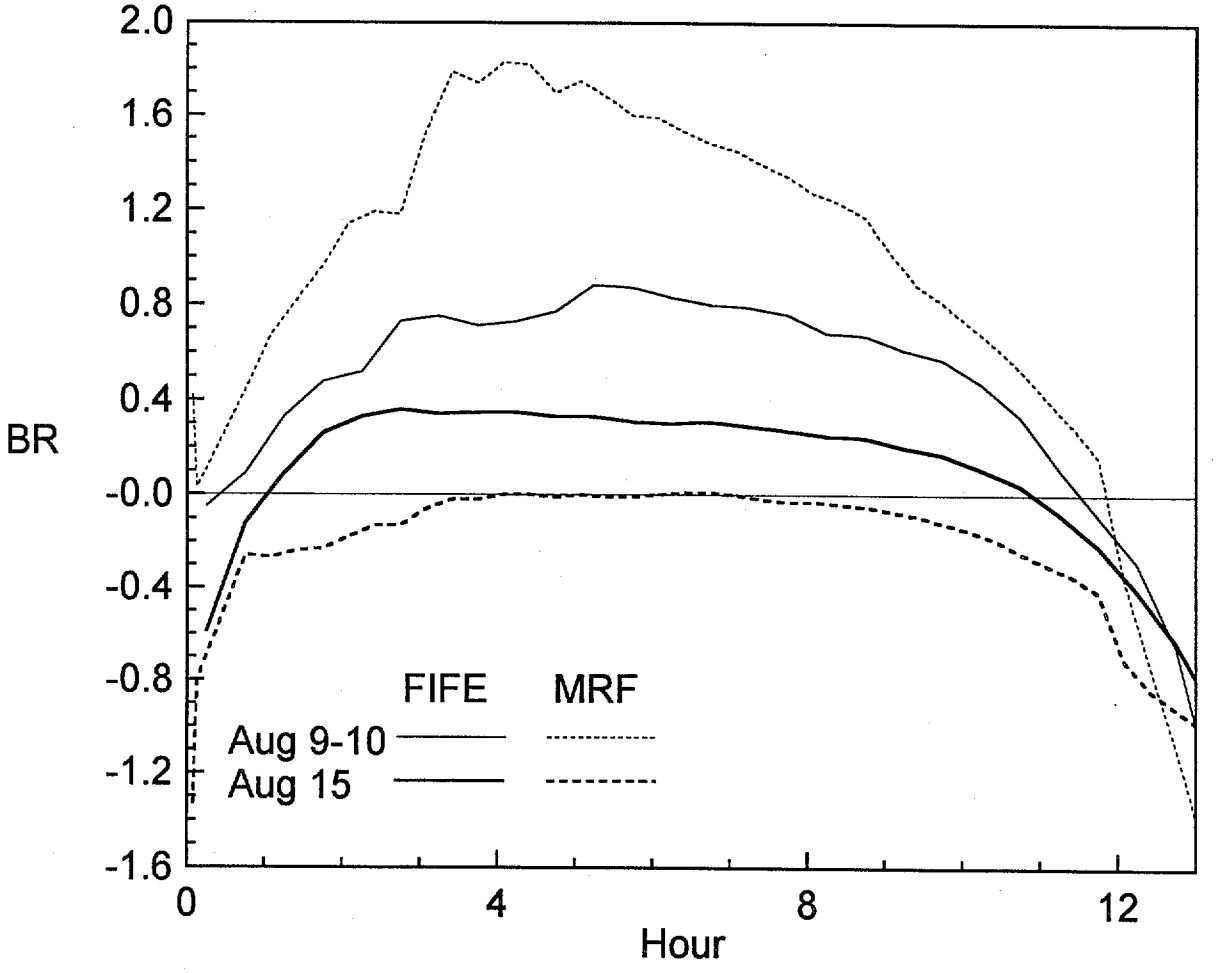

Jul 12 1995

_FIG24_HDF

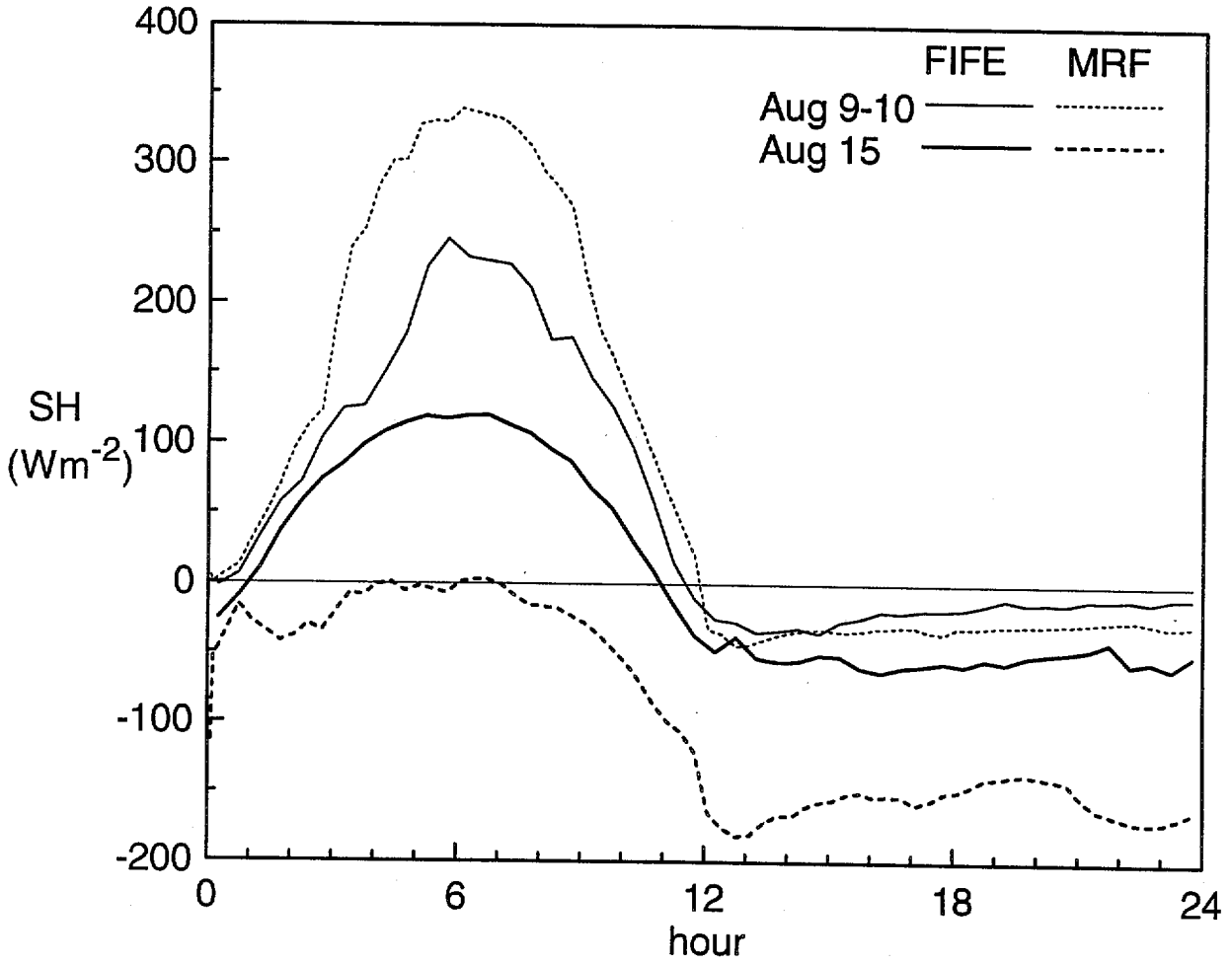

Jul 12 1995

_FIG25_HDF

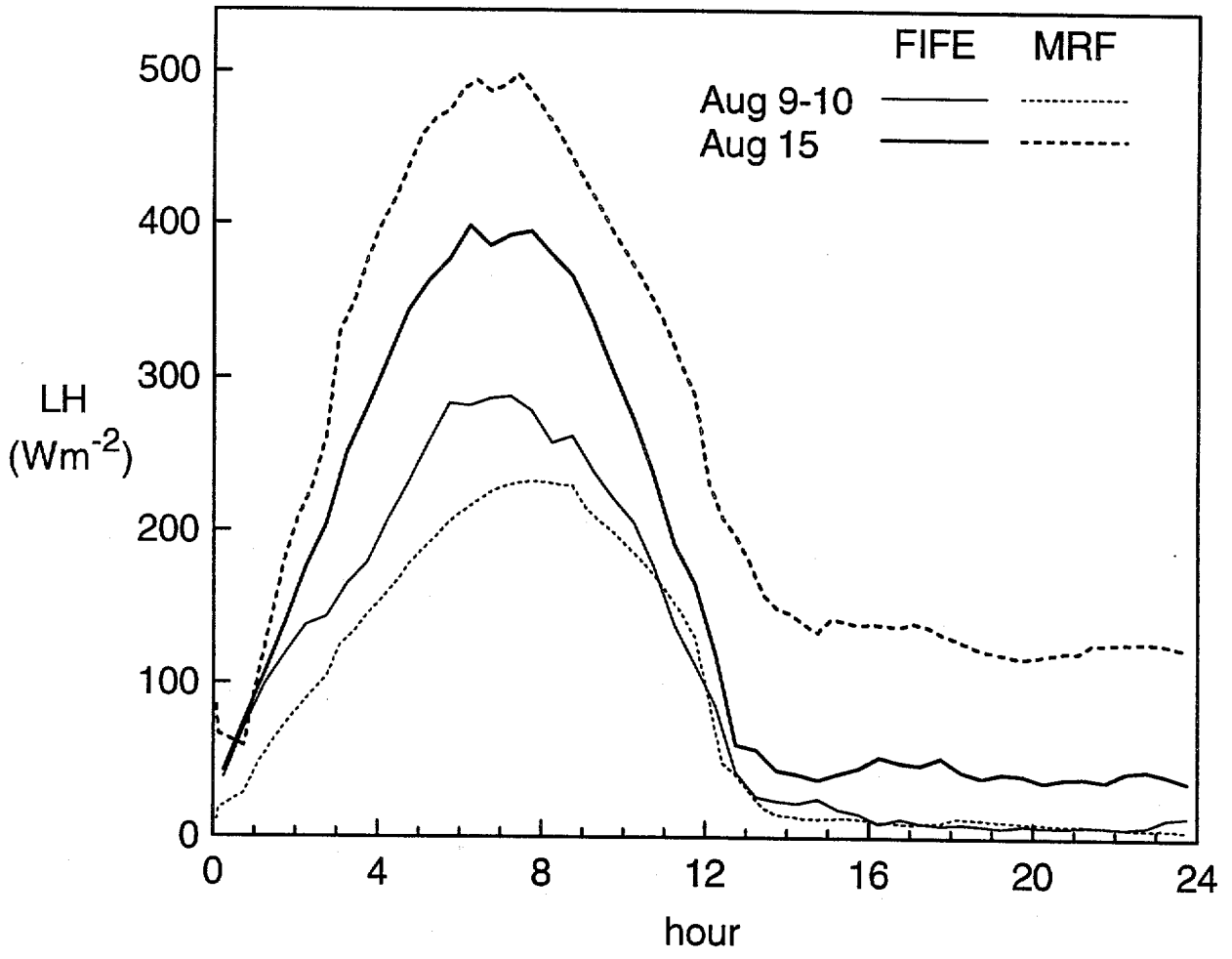

Jul. 12 1995

_FIG26_HDF

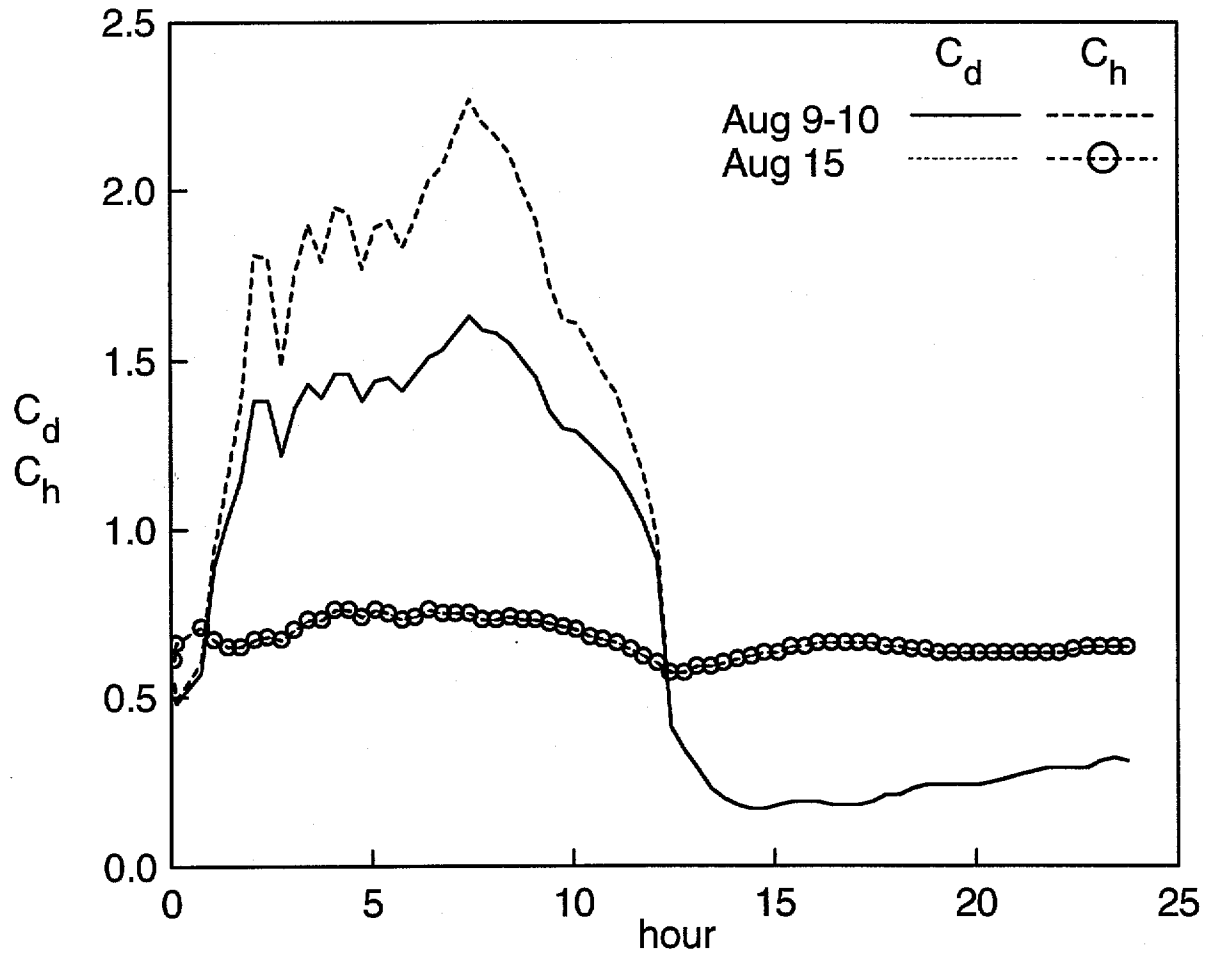

Jul 13 1995

FIG27_HDF

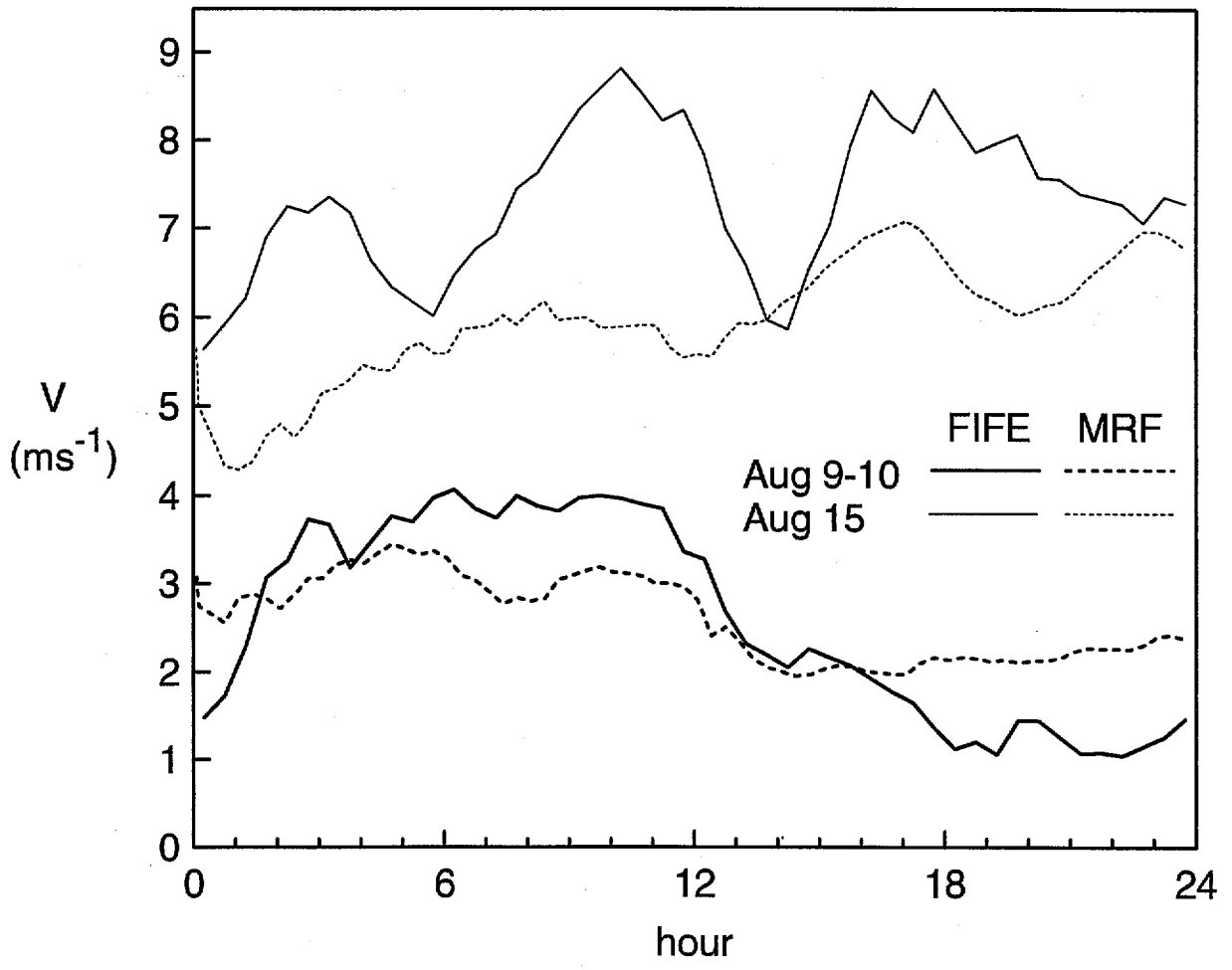

Jul 13 1995

FIG28_HDF

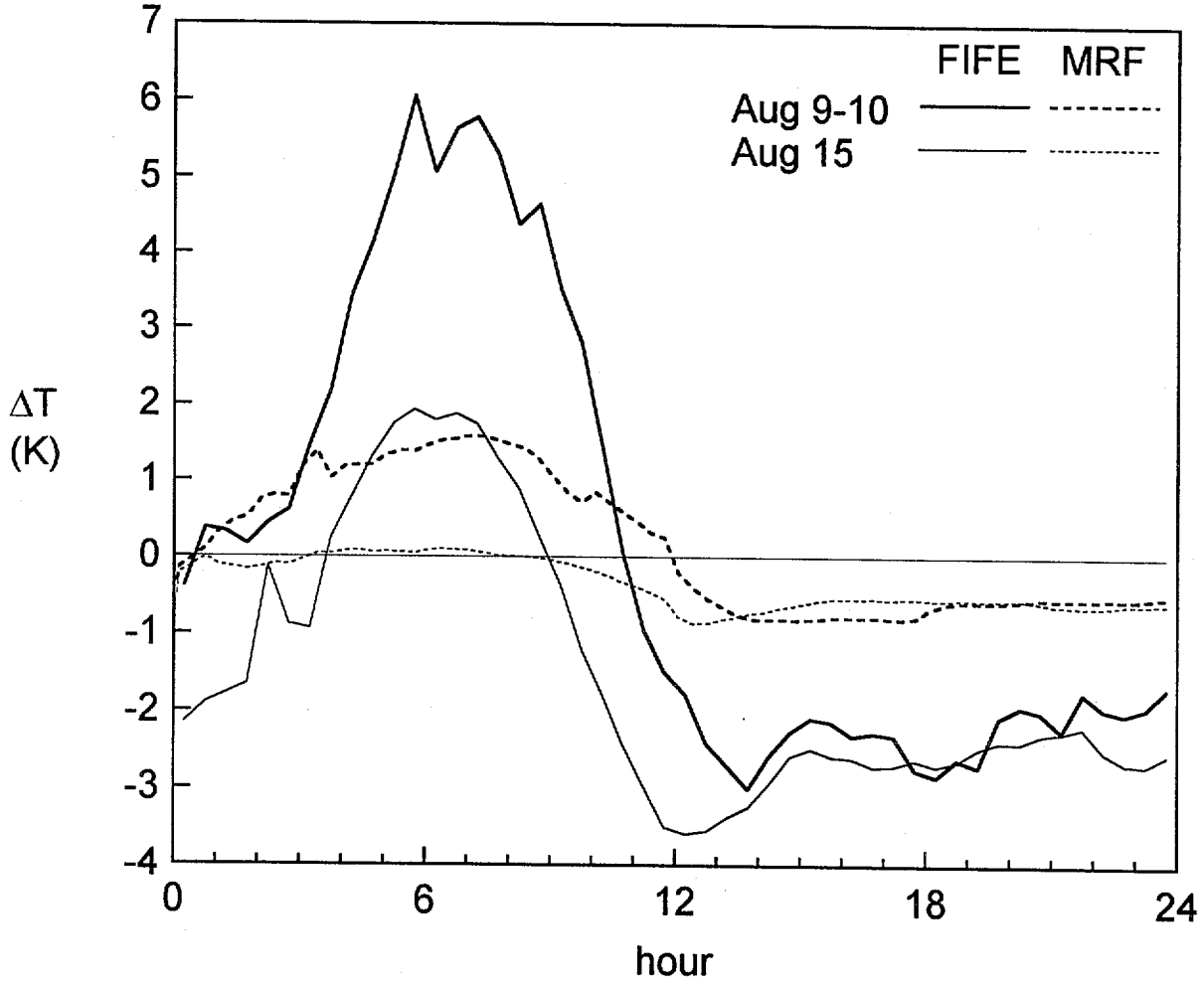

Jul. 12 1995

FIG29_HDF

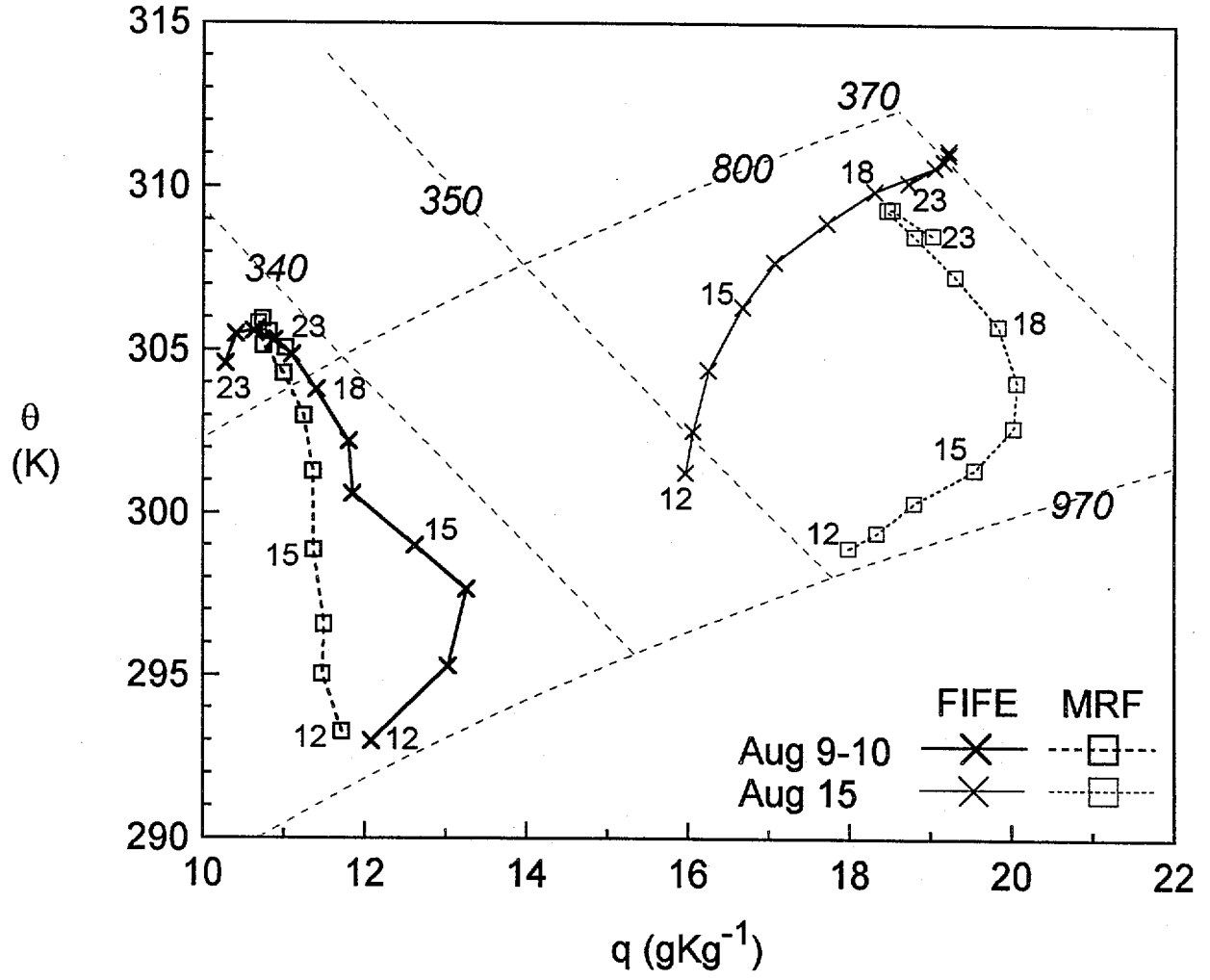

Jul. 12 1995

FIG30_HDF

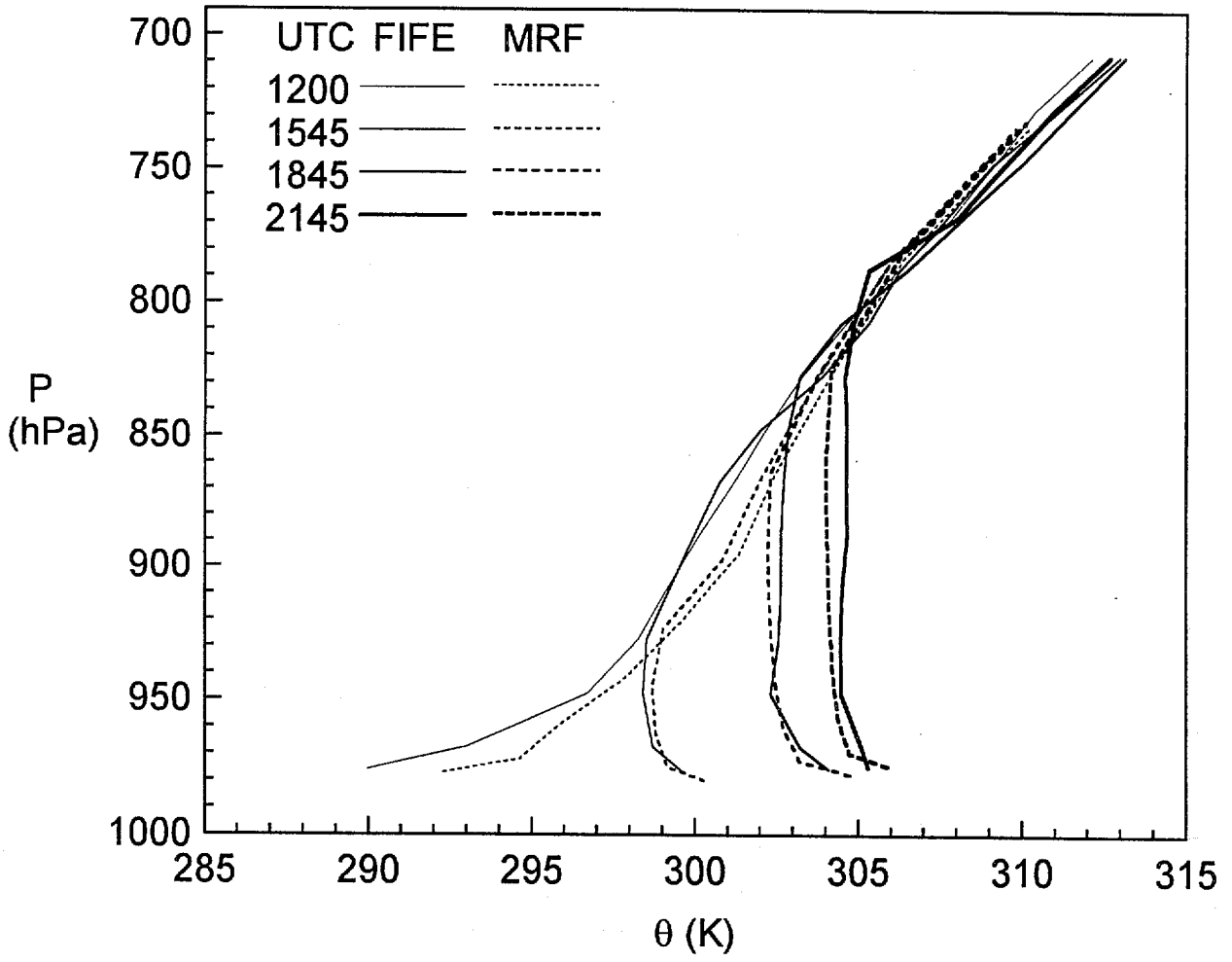

Jul. 12 1995

FIG31A_HDF

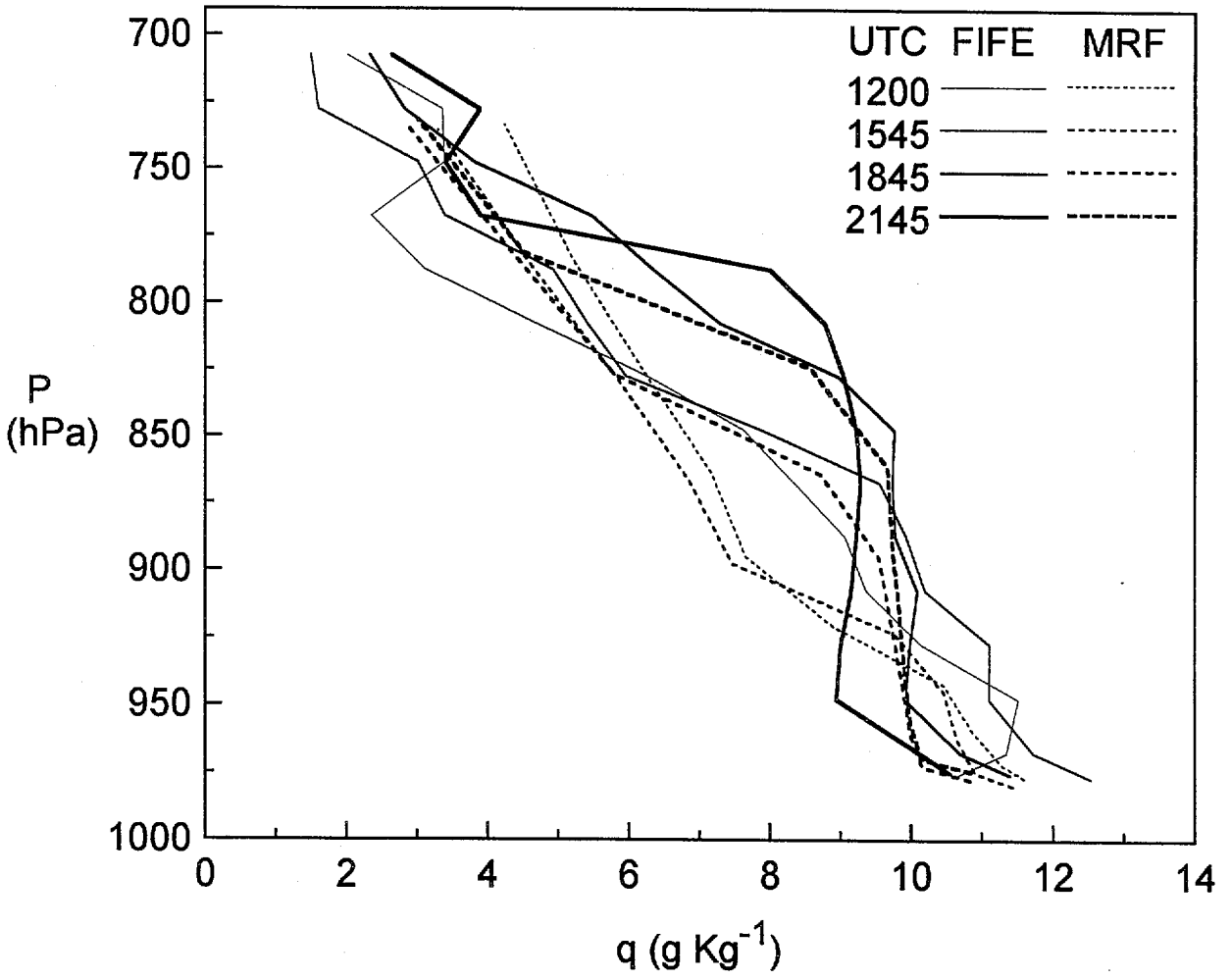

Jul. 12 1995

FIG31B_HDF

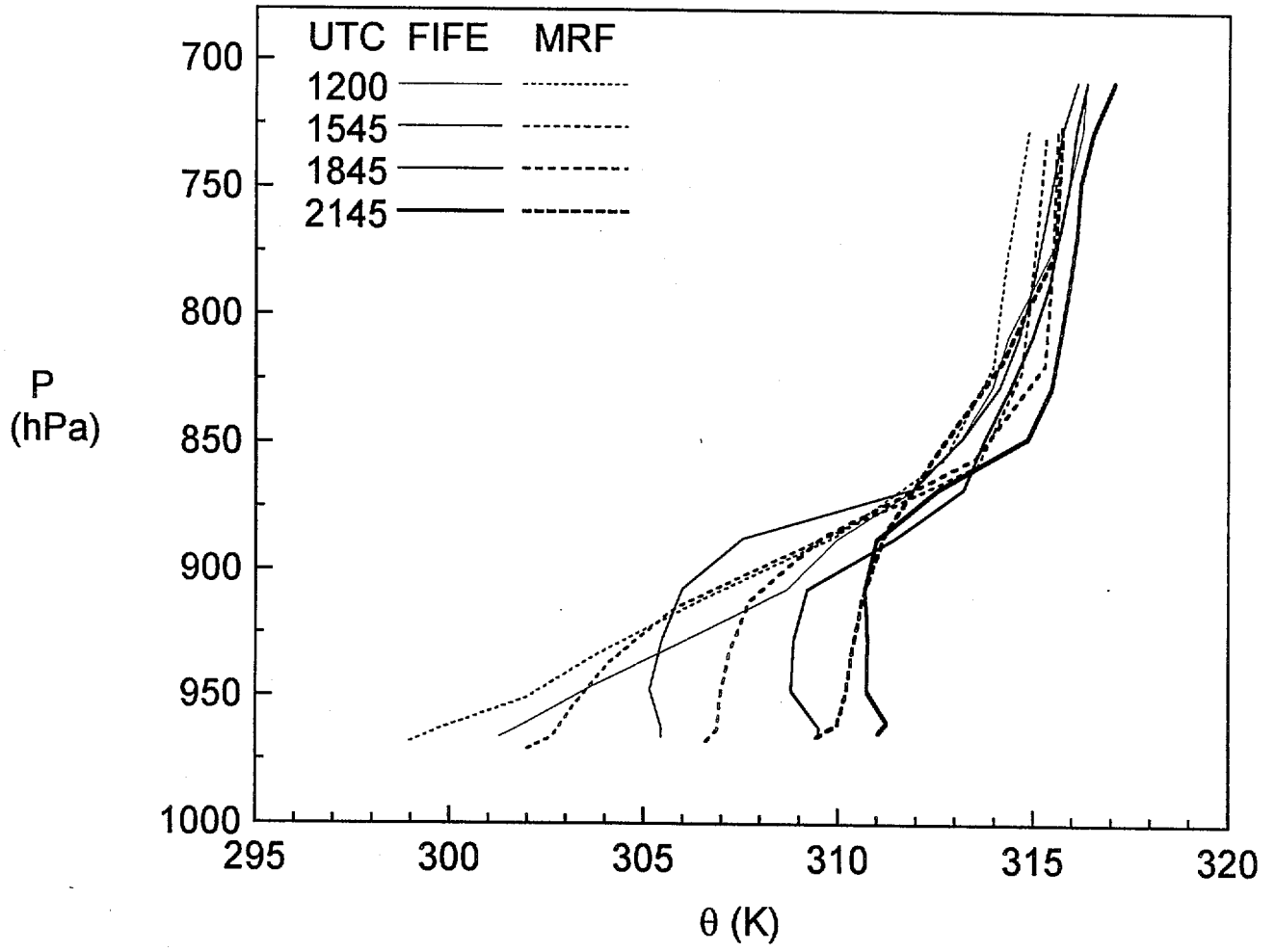

Jul. 12 1995

FIG32A_HDF

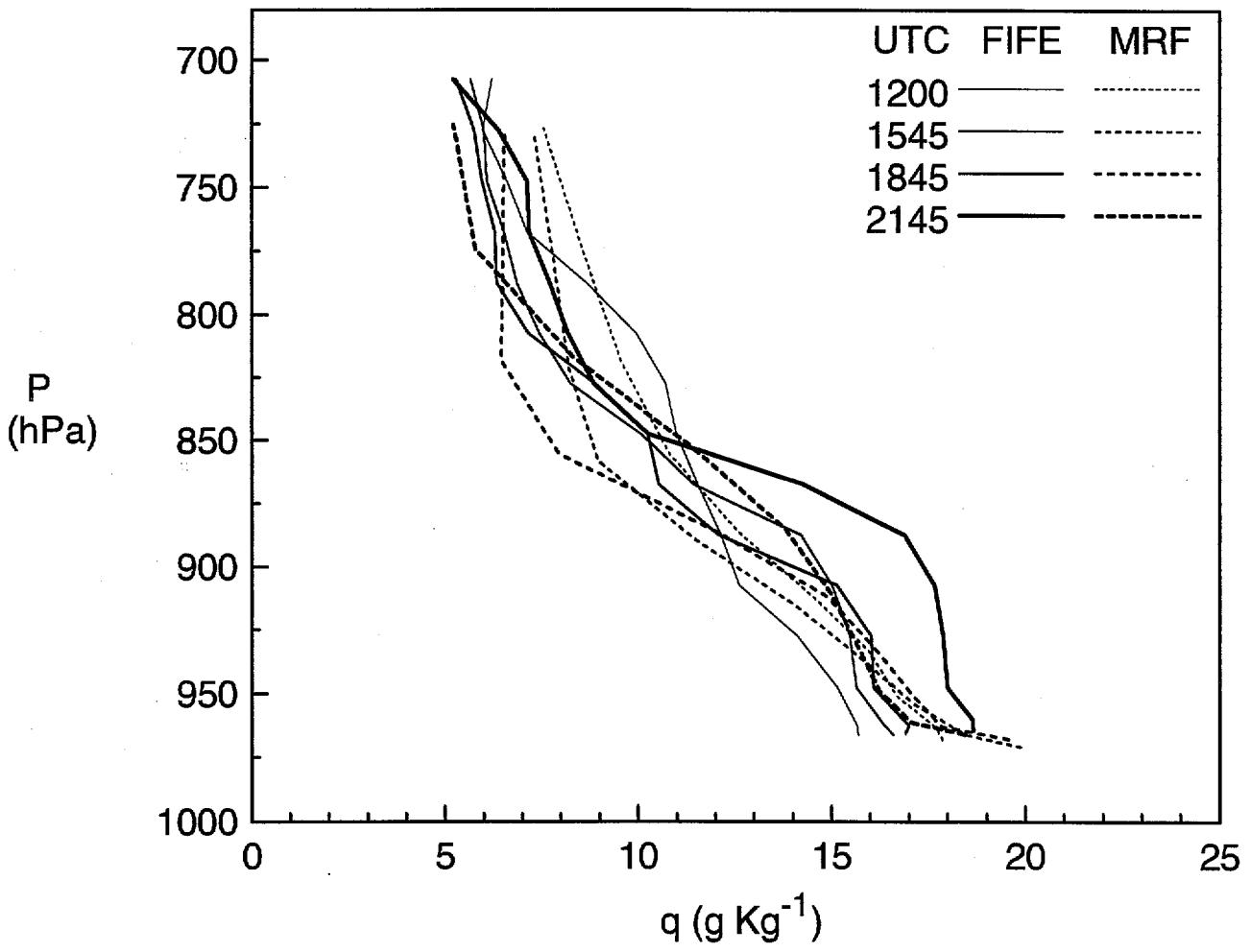

Jul 13 1995

FIG32B_HDF

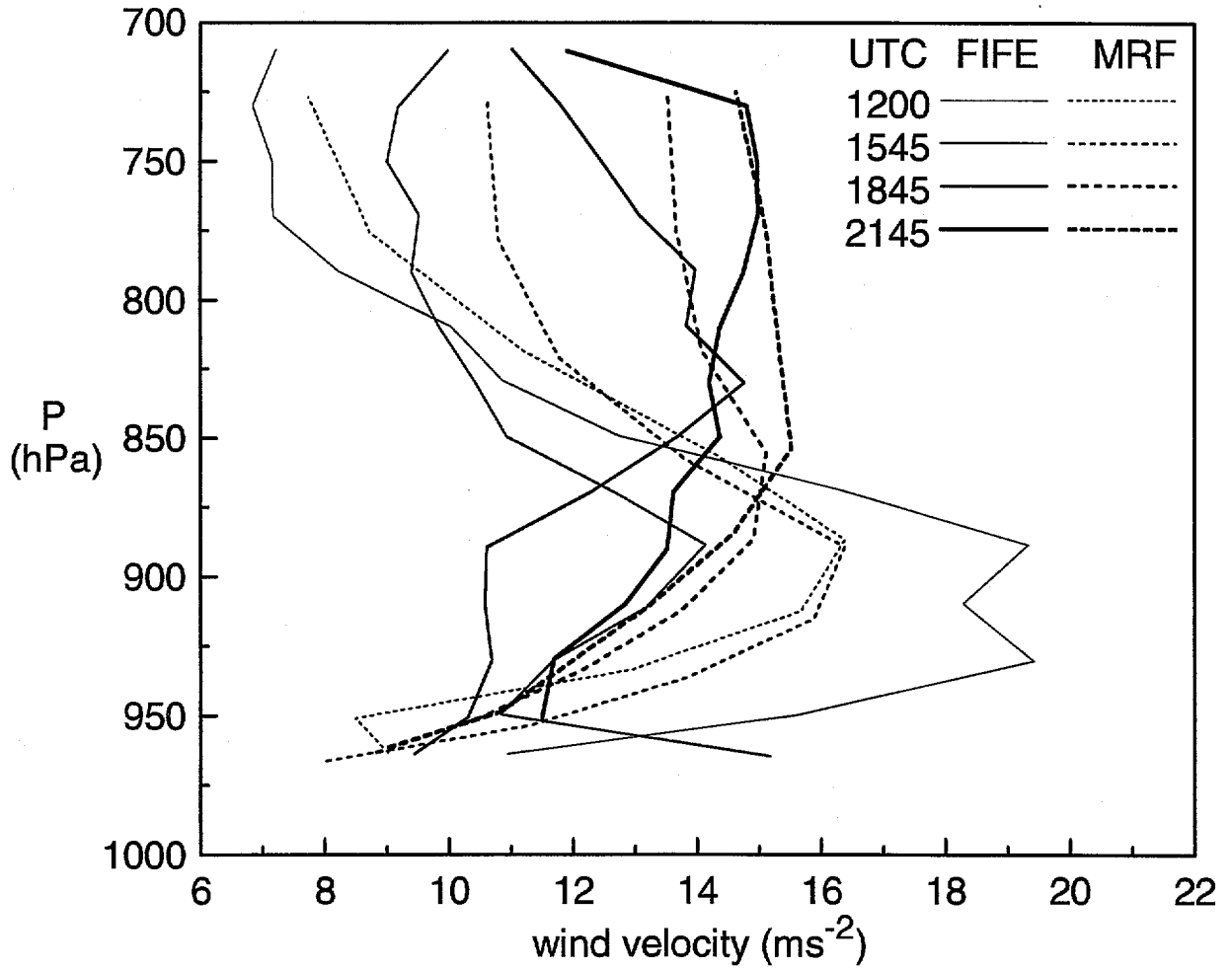

Jul 13 1995

FIG33_HDF

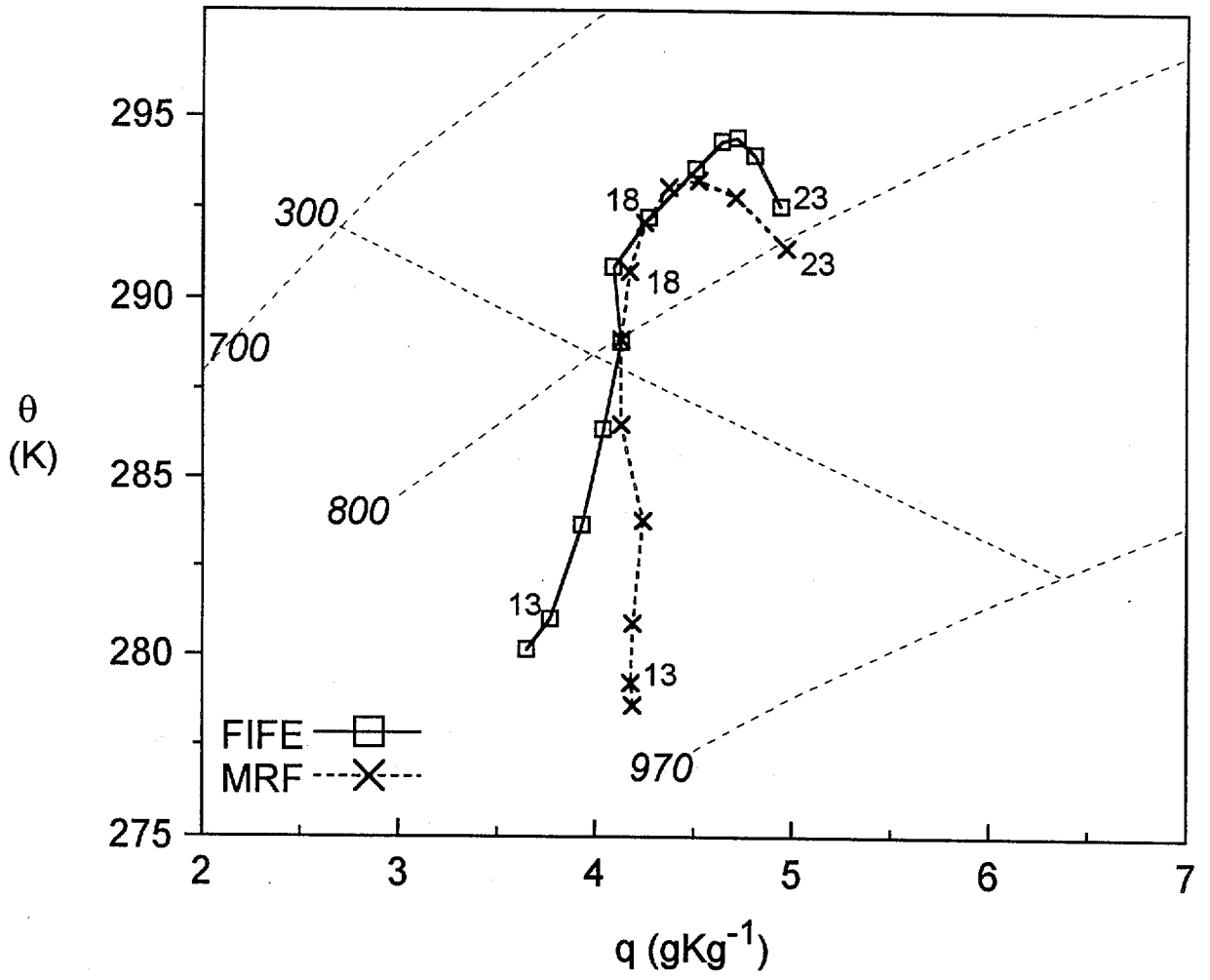

Jul. 12 1995

FIG34_HDF

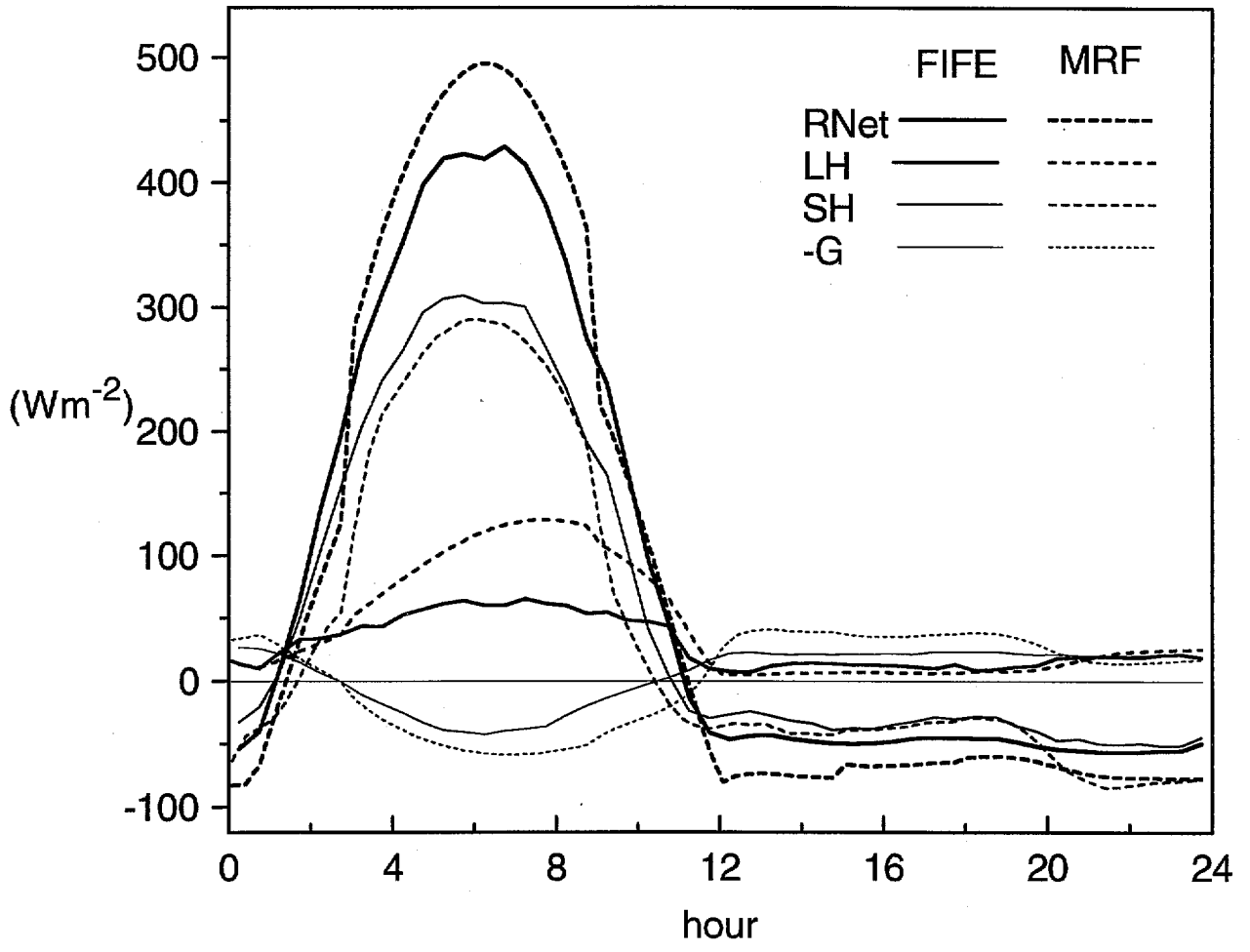

Jul 13 1995

FIG35_HDF

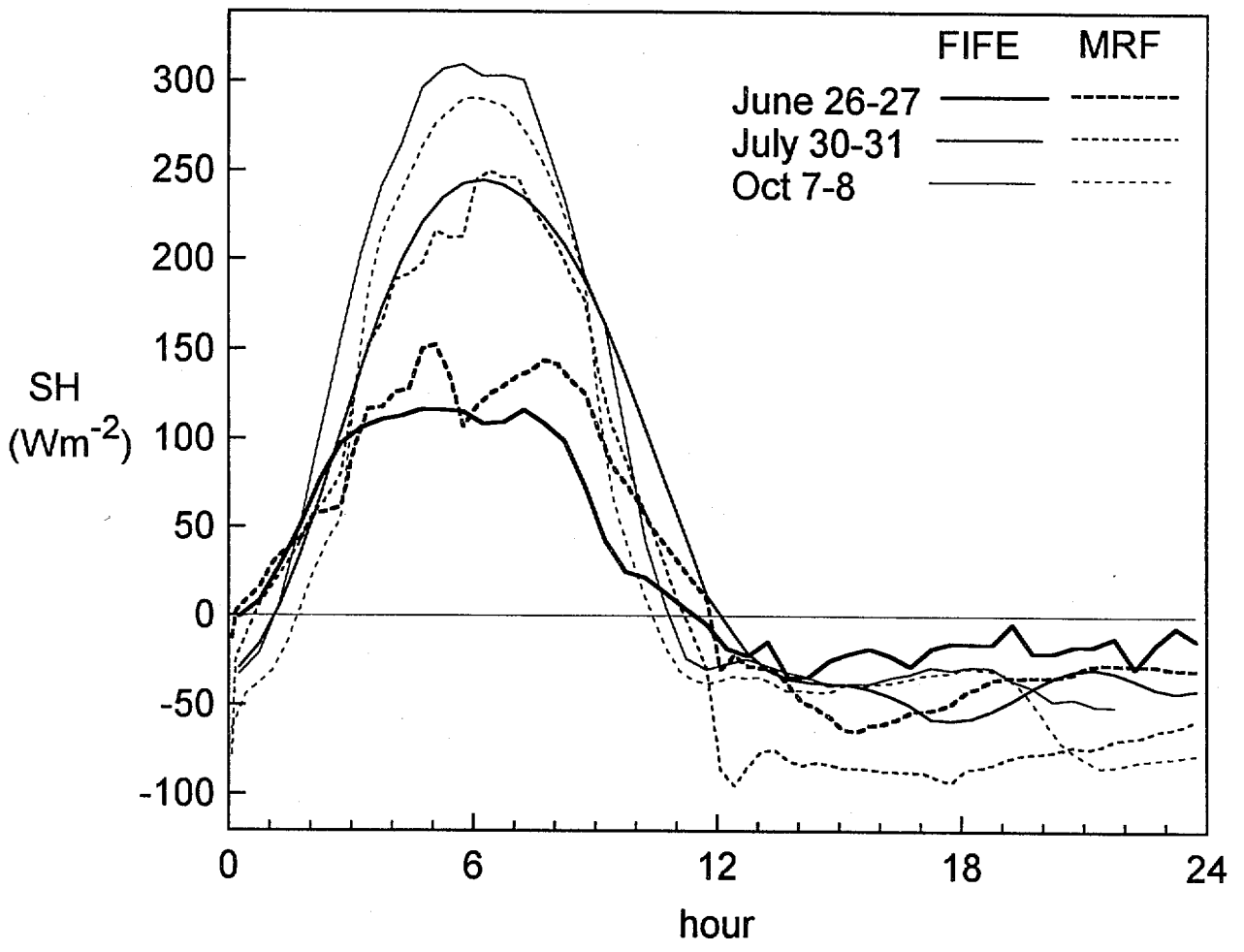

Jul. 12 1995

FIG36_HDF

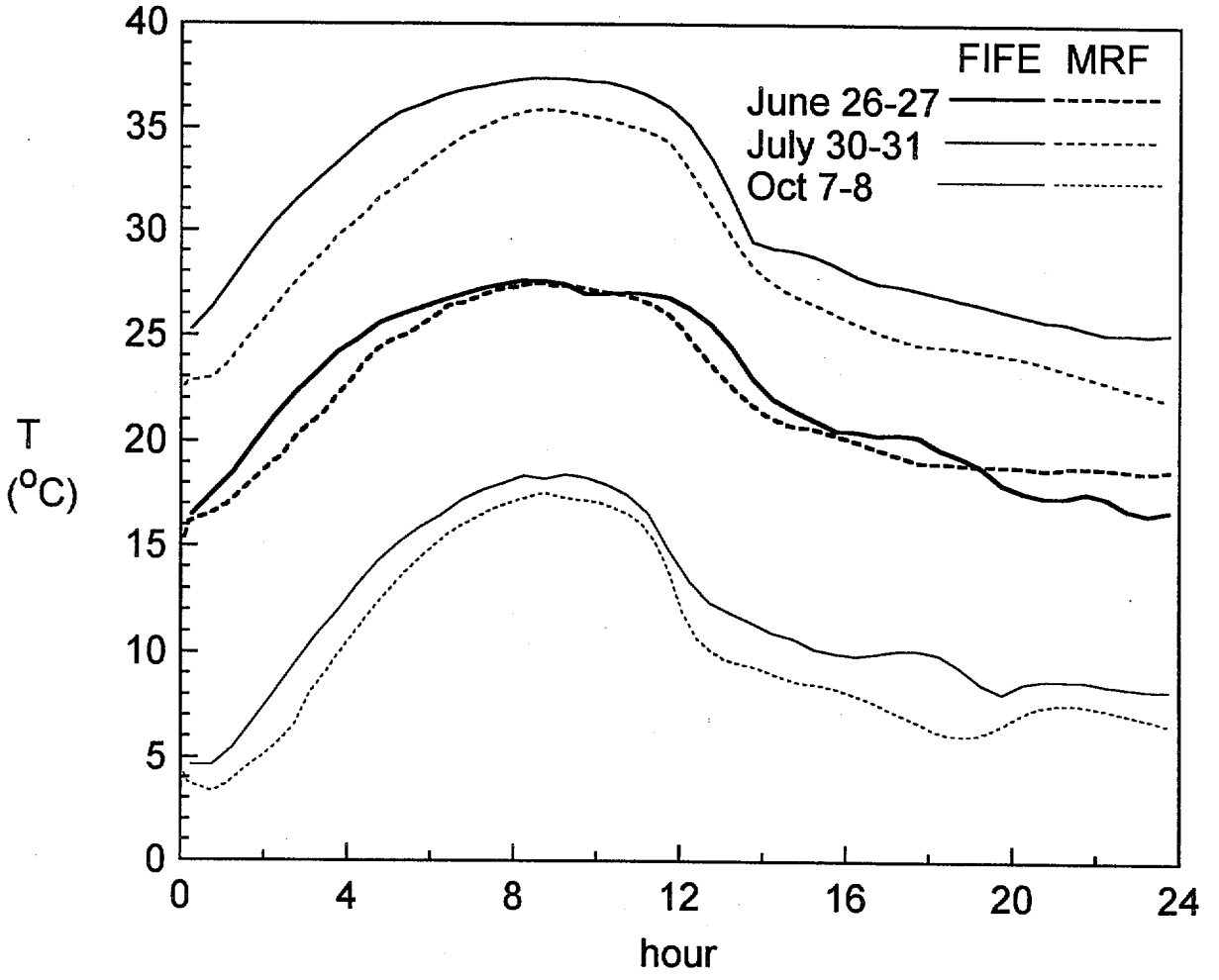

Jul. 17 1995

FIG37_HDF